Finite volume evolution Galerkin method for hyperbolic conservation laws with spatially varying flux functions

K.R. Arun [a], M. Kraft [b], M. Lukáčová-Medvid'ová [b,*], Phoolan Prasad [a]

[a] *Indian Institute of Science, Bangalore, India*
[b] *Institute of Numerical Simulation, Hamburg University of Technology, Schwarzenbergstrasse 95, Hamburg 21073, Germany*

ARTICLE INFO

ABSTRACT

We present a generalization of the finite volume evolution Galerkin scheme [M. Lukáčová-Medvid'ová, J. Saibertov'a, G. Warnecke, Finite volume evolution Galerkin methods for non-linear hyperbolic systems, J. Comp. Phys. (2002) 183 533– 562; M. Lukáčová-Medvid'ová, K.W. Morton, G. Warnecke, Finite volume evolution Galerkin (FVEG) methods for hyperbolic problems, SIAM J. Sci. Comput. (2004) 26 1–30] for hyperbolic systems with spatially varying flux functions. Our goal is to develop a genuinely multi-dimensional numerical scheme for wave propagation problems in a heterogeneous media. We illustrate our methodology for acoustic waves in a heterogeneous medium but the results can be generalized to more complex systems. The finite volume evolution Galerkin (FVEG) method is a predictor–corrector method combining the finite volume corrector step with the evolutionary predictor step. In order to evolve fluxes along the cell interfaces we use multi-dimensional approximate evolution operator. The latter is constructed using the theory of bicharacteristics under the assumption of spatially dependent wave speeds. To approximate heterogeneous medium a staggered grid approach is used. Several numerical experiments for wave propagation with continuous as well as discontinuous wave speeds confirm the robustness and reliability of the new FVEG scheme.

1. Introduction

Hyperbolic conservation laws with spatially varying fluxes arise in many practical applications. For example, in modelling of acoustic, electromagnetics or elastic waves in heterogeneous materials or in the traffic flow with varying conditions. In exploration seismology one studies the propagation of small amplitude of man made waves in earth and their reflection off geological structures. For numerical modelling of wave propagation in heterogeneous media the reader is referred, for example, to [1,8–10,14,23] and the references therein. A large variety of finite difference schemes for wave propagation can be found in particular in seismological literature; see, e.g., [2,3,7,12,24,33,34] just to mention some of them.

Our aim in this paper is to develop a new genuinely multi-dimensional method for approximation of hyperbolic conservation laws with spatially varying fluxes using the so-called evolution Galerkin framework. In particular, we will illustrate the methodology for the wave equation system with spatially varying wave speeds and simulate the propagation of acoustic

---

waves in heterogeneous media. In our future study we would like to generalize ideas presented here to other models, for example for linear elastic waves.

The evolution (or characteristic) Galerkin schemes were first derived by Morton, Süli and their collaborators for scalar problems and for one-dimensional systems, see [15,16] and the references therein. This research was motivated by the pioneering work of Butler [4] and the related works of Prasad et al. [31,32]. In 2000 Lukáčová-Medvid'ová, Morton and Warnecke derived the Evolution Galerkin schemes for the linear wave equation system with constant wave speed [17]. In the recent works of Lukáčová-Medvid'ová et al. [11,18–20] a genuinely multi-dimensional finite volume evolution Galerkin (FVEG) method has been developed. The FVEG scheme can be viewed as a predictor–corrector method; in the predictor step the data are evolved along the bicharacteristics to determine the approximate solution at cell interfaces. In the corrector step the finite volume update in conservative variables is realized. The method works well for linear as well as nonlinear hyperbolic systems. In order to derive evolution operators for nonlinear systems a suitable local linearization has been used. For a locally linearized system bicharacteristics are reduced to straight lines.

The goal of this paper is to derive the FVEG scheme for linear hyperbolic systems with spatially varying flux functions without any local linearization. In this case the Jacobians are spatially varying but time independent and bicharacteristics are no longer straight lines. This introduces new difficulties in the derivation of the exact integral representation as well as in the numerical approximation. In particular, we consider the acoustic wave equation system with a variable wave speed. The results presented here can be generalized to more complex hyperbolic conservation laws. However, we should note that an important property of our model is the fixed number of positive eigenvalues; indeed, as we will see in Section 2 eigenvalues do not pass through zero. Consequently, we are not facing the difficulties with development of delta functions as it might happen in a general case.

A mathematical model for propagation of acoustic waves can be derived from the conservative form of the Euler equations. One considers small perturbations of the background steady state ρ_0, u_0, v_0, p_0, where ρ_0, u_0, v_0, p_0 denote respectively the density, x, y-components of velocity and pressure. For simplicity, we assume that the gas is at rest initially, i.e. $u_0 = 0 = v_0$. It turns out from momentum equations of the Euler equations that p_0 has to be a constant. The acoustic waves are then governed by the following first order system, cf., e.g., [8]:

$$\begin{bmatrix} p \\ \rho_0 u \\ \rho_0 v \end{bmatrix}_t + \begin{bmatrix} \gamma p_0 u \\ p \\ 0 \end{bmatrix}_x + \begin{bmatrix} \gamma p_0 v \\ 0 \\ p \end{bmatrix}_y = 0. \tag{1.1}$$

Equivalently we have

$$\boldsymbol{u}_t + (\boldsymbol{f}_1(\boldsymbol{u}))_x + (\boldsymbol{f}_2(\boldsymbol{u}))_y = 0, \tag{1.2}$$

where

$$\boldsymbol{u} = \begin{bmatrix} p \\ \rho_0 u \\ \rho_0 v \end{bmatrix}, \quad \boldsymbol{f}_1(\boldsymbol{u}) = \begin{bmatrix} a_0^2 \rho_0 u \\ p \\ 0 \end{bmatrix}, \quad \boldsymbol{f}_2(\boldsymbol{u}) = \begin{bmatrix} a_0^2 \rho_0 v \\ 0 \\ p \end{bmatrix}$$

and $a_0 = \sqrt{\gamma p_0/\rho_0}$ denotes the wave speed. We use (1.2) as our starting point.

In differential form this reads

$$\boldsymbol{v}_t + \boldsymbol{A}_1 \boldsymbol{v}_x + \boldsymbol{A}_2 \boldsymbol{v}_y = 0, \tag{1.3}$$

where $\boldsymbol{v} = \begin{bmatrix} p \\ u \\ v \end{bmatrix}$, $\boldsymbol{A}_1 = \begin{bmatrix} 0 & \gamma p_0 & 0 \\ \frac{1}{\rho_0} & 0 & 0 \\ 0 & 0 & 0 \end{bmatrix}$, $\boldsymbol{A}_2 = \begin{bmatrix} 0 & 0 & \gamma p_0 \\ 0 & 0 & 0 \\ \frac{1}{\rho_0} & 0 & 0 \end{bmatrix}$. Note that $\rho_0 = \rho_0(x,y)$ and $p_0 \equiv$ const. We develop the FVEG

method for the system of conservation laws (1.4) in which the flux functions are non-constant functions of x and y.

The paper is organized as follows: in Section 2 we start with a brief review of characteristic theory in multi-dimensions to define the bicharacteristics of the wave equation system (1.3) and derive the exact integral representation along the bicharacteristics. In Section 3 the exact integral equations are approximated by numerical quadratures and suitable approximate evolution operators are derived. In Section 4 the first and second order finite volume evolution Galerkin scheme are constructed. We will show that it is preferable to model the heterogeneous medium by means of a staggered grid. In fact we approximate the wave speed and the impedance on a staggered grid. Finally, in Section 5 we illustrate the behaviour of the presented scheme on a set of numerical experiments for wave equation system with continuous as well as discontinuous wave speeds.

2. Bicharacteristics and exact integral representation

A characteristic surface $\Omega : \varphi(x, y, t) = 0$ of (1.3) is a possible surface of discontinuity in the first order derivatives of $\boldsymbol{v}$. The evolution of the surface Ω is given by the eikonal equation

$$F(x, y, t, \varphi_x, \varphi_y, \varphi_t) \equiv \det(\boldsymbol{I}\varphi_t + \boldsymbol{A}_1\varphi_x + \boldsymbol{A}_2\varphi_y) = 0, \tag{2.1}$$

where $\boldsymbol{I}$ is the 3×3 identity matrix. Note that (2.1) is a scalar differential equation for φ. The characteristic curves of (2.1) are called the bicharacteristic curves of (1.3). These are curves in the (x, y, t) space and can be obtained by solving the Charpit's equations, cf. [28]

$$\frac{dt}{d\sigma} = F_q, \quad \frac{dx}{d\sigma} = F_{p_1}, \quad \frac{dy}{d\sigma} = F_{p_2},$$
$$\frac{dq}{d\sigma} = -F_t, \quad \frac{dp_1}{d\sigma} = -F_x, \quad \frac{dp_2}{d\sigma} = -F_y, \tag{2.2}$$

where $p_1 = \varphi_x$, $p_2 = \varphi_y$ and $q = \varphi_t$. A bicharacteristic curve in (x, t)-space is a solution $(x(\sigma), y(\sigma), t(\sigma), p_1(\sigma), p_2(\sigma), q(\sigma))$ of (2.2) satisfying the relation

$$Fx(\sigma), y(\sigma), t(\sigma), p_1(\sigma), p_2(\sigma), q(\sigma) = 0. \tag{2.3}$$

From the theory of first order partial differential equations it follows that a characteristic surface $\Omega : \varphi(x, y, t) = 0$ of (1.3) is generated by a one parameter family of bicharacteristic curves. We consider a special characteristic surface, namely the backward *characteristic conoid*, generated by all bicharacteristic curves passing a point $P = (x, y, t + \Delta t)$. Our aim is to derive an expression for the solution of (1.3) at the point $P(x, y, t + \Delta t)$ in terms of the solution at a point $Q(x(t), y(t), t)$ lying on the base of the above characteristic conoid at the level t.

From (2.1) and (2.3) it can be seen that for any fixed choice of (p_1, p_2) the relation (2.3) can be satisfied by three possible values of q which are precisely the eigenvalues of matrix pencil $p_1\boldsymbol{A}_1 + p_2\boldsymbol{A}_2$. Hence the system (1.3) possess three families of bicharacteristics. It follows from the bicharacteristic Eq. (2.2) that two families of bicharacteristics coincides if they correspond to two values of (p_1, p_2) which differ only by a constant factor. Thus, it is enough to consider (p_1, p_2) with $p_1^2 + p_2^2 = 1$. In what follows we take $p_1 = \cos\theta, p_2 = \sin\theta$ and denote $\boldsymbol{n}(\theta) = (\cos\theta, \sin\theta), \theta \in [0, 2\pi]$. The matrix pencil $\boldsymbol{A} := \cos\theta\boldsymbol{A}_1 + \sin\theta\boldsymbol{A}_2$ has three eigenvalues $\lambda_1 = -a_0, \lambda_2 = 0, \lambda_3 = a_0, a_0 > 0$, and a full set of left and right eigenvectors.

$$\boldsymbol{l}_1 = \tfrac{1}{2}\left(-\tfrac{1}{a_0\rho_0}, \cos\theta, \sin\theta\right), \quad \boldsymbol{l}_2 = (0, \sin\theta, -\cos\theta), \quad \boldsymbol{l}_3 = \tfrac{1}{2}\left(\tfrac{1}{a_0\rho_0}, \cos\theta, \sin\theta\right).$$
$$\boldsymbol{r}_1 = \begin{bmatrix} -a_0\rho_0 \\ \cos\theta \\ \sin\theta \end{bmatrix}, \quad \boldsymbol{r}_2 = \begin{bmatrix} 0 \\ \sin\theta \\ \cos\theta \end{bmatrix}, \quad \boldsymbol{r}_3 = \begin{bmatrix} a_0\rho_0 \\ \cos\theta \\ \sin\theta \end{bmatrix}. \tag{2.4}$$

As mentioned above the envelope of the bicharacteristics passing through a fixed point in space–time is called a characteristic conoid, see Fig. 1; cf. also [17–22], where the notion bicharacteristic cone have been used in a special case of systems with constant Jacobians. Let us consider the lower part of the characteristic conoid at the point P. Then a wavefront is the projection on the (x, y)-space of the section of the characteristic conoid by a hyperplane $t = \text{const}$. The vector $\boldsymbol{n}(\theta)$ at any point determines a unit normal direction to the wavefront, see Fig. 2. A ray is the projection of a bicharacteristic curve onto the (x, y)-space. Therefore a wavefront is the locus of the tip of the rays. The velocity of these moving points in the plane is called a ray velocity [5], [28]. For the system (1.3) these ray velocities corresponding to the three bicharacteristic fields can be determined to be

$$\boldsymbol{\chi}_1 = (-a_0\cos\theta, -a_0\sin\theta), \quad \boldsymbol{\chi}_2 = (0, 0), \quad \boldsymbol{\chi}_3 = (a_0\cos\theta, a_0\sin\theta).$$
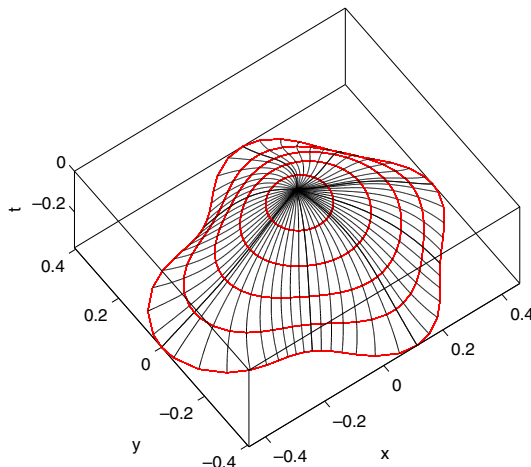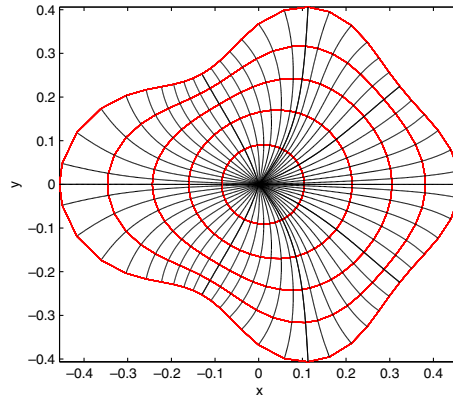

Fig. 1. Characteristic conoid.

Fig. 2. Wavefronts and rays.

Time evolution of the rays $(x(t), y(t))$ and of the normal vector $\boldsymbol{n}(\theta(t))$ can be obtained using the extended lemma on bicharacteristics [29]

$$\frac{\mathrm{d}x}{\mathrm{d}t} = -a_0(x,y)\cos\theta, \quad \frac{\mathrm{d}y}{\mathrm{d}t} = -a_0(x,y)\sin\theta, \quad \frac{\mathrm{d}\theta}{\mathrm{d}t} = -a_{0x}\sin\theta + a_{0y}\cos\theta,$$

$$\frac{\mathrm{d}x}{\mathrm{d}t} = 0, \quad \frac{\mathrm{d}y}{\mathrm{d}t} = 0, \quad \frac{\mathrm{d}\theta}{\mathrm{d}t} = 0,$$ (2.5)

$$\frac{\mathrm{d}x}{\mathrm{d}t} = a_0(x,y)\cos\theta, \quad \frac{\mathrm{d}y}{\mathrm{d}t} = a_0(x,y)\sin\theta, \quad \frac{\mathrm{d}\theta}{\mathrm{d}t} = a_{0x}\sin\theta - a_{0y}\cos\theta, \quad \theta \in [0, 2\pi].$$

For the wave equation system with constant sound speed $a_0(x,y) \equiv$ const. the bicharacteristic Eq. (2.5) can be solved immediately to get the bicharacteristics to be straight lines. In Appendix A we derive the solution of the ray Eq. (2.5) and draw the corresponding characteristic conoid in the case when $a_0(x,y)$ is a linear function of x, y. Note that in general the geometry of the characteristic conoid can be quite complicated, see Figs. 1 and 2. Here the characteristic conoid is obtained by solving the ray Eq. (2.5) with $a_0(x,y) = 1 + \frac{1}{4}(\sin(4\pi x) + \cos(4\pi x))$.

Any solution of (2.5) may be represented as $x = x(t, \omega)$, $y = y(t, \omega)$, $\theta = \theta(t, \omega)$. Here $\omega = \theta(t_{n+1}) \in [0, 2\pi]$ is a parameter and $\omega =$ const. represents a particular bicharacteristic. From this representation it is clear that the wavefront can be parameterized by ω. Again, we can see easily from the ray Eq. (2.5) that the third family of bicharacteristics is equivalent to the first family up to a rotation of the angle θ by π. Hence, the first and third family of bicharacteristics create the same characteristic conoid. The second family of bicharacteristics degenerates to a single line. Thus in our integral representation below it will be enough to consider the first and second bicharacteristic fields. For the wave equation system (1.3) the transport equations along the three families of bicharacteristics [27], [28] can be obtained to be

$$\frac{\mathrm{d}p}{\mathrm{d}t} - z_0\cos\theta\frac{\mathrm{d}u}{\mathrm{d}t} - z_0\sin\theta\frac{\mathrm{d}v}{\mathrm{d}t} + z_0 S = 0$$ (2.6)

$$z_0\sin\theta\frac{\mathrm{d}u}{\mathrm{d}t} - z_0\cos\theta\frac{\mathrm{d}v}{\mathrm{d}t} + a_0(p_x\sin\theta - p_y\cos\theta) = 0$$ (2.7)

$$\frac{\mathrm{d}p}{\mathrm{d}t} + z_0\cos\theta\frac{\mathrm{d}u}{\mathrm{d}t} + z_0\sin\theta\frac{\mathrm{d}v}{\mathrm{d}t} + z_0 S = 0,$$ (2.8)

where $z_0 = a_0\rho_0$ is the impedance of the medium and S is a source term arising from the multi-dimensionality of the hyperbolic system

$$S := a_0\{u_x\sin^2\theta - (u_y + v_x)\sin\theta\cos\theta + v_y\cos^2\theta\}.$$ (2.9)

In the transport Eqs. (2.6),(2.7),(2.8) the jth equation is valid only along the jth family of bicharacteristics, $j = 1, 2, 3$. Our aim is to derive an evolution operator for the wave equation system (1.3). Fix a point $P = (x, y, t_n + \Delta t)$ and consider the characteristic conoid with P as the apex. Let $Q_j = Q_j(x(t_n), y(t_n), t_n)$, $\widetilde{Q}_j = \widetilde{Q}_j(x(\tau), y(\tau), \tau)$, $j = 1, 2, 3$, be respectively the footpoints of the jth family of bicharacteristics on the planes $t = t_n$ and $t = \tau \in (t_n, t_{n+1})$ (for simplicity we have denoted $x(t_n, \omega), y(t_n, \omega), x(\tau, \omega), y(\tau, \omega)$ by $x(t_n), y(t_n), x(\tau)$ and $y(\tau)$, respectively). We integrate the transport Eq. (2.6),(2.7),(2.8) along the respective bicharacteristics and take an integral average over the wavefronts. Integrating (2.6) in time from t_n to t_{n+1} and using the integration by parts for the second and third terms yield

$$p(P) = p(Q_1) + \cos\omega(z_0 u)(P) - \cos\theta(z_0 u)(Q_1) - \int_{t_n}^{t_{n+1}} (z_0 a_{0x} u)(\widetilde{Q}_1)\mathrm{d}\tau + \sin\omega(z_0 v)(P) - \sin\theta(z_0 v)(Q_1)$$

$$- \int_{t_n}^{t_{n+1}} (z_0 a_{0y} v)(\widetilde{Q}_1)\mathrm{d}\tau - \int_{t_n}^{t_{n+1}} (z_0 S)(\widetilde{Q}_1)\mathrm{d}\tau.$$ (2.10)

Integrate (2.10) over $\omega \in [0, 2\pi]$ and divide by 2π to obtain

$$p(P) = \frac{1}{2\pi} \int_0^{2\pi} (p - z_0 u \cos\theta - z_0 v \sin\theta)(Q_1)d\omega - \frac{1}{2\pi} \int_0^{2\pi} \int_{t_n}^{t_{n+1}} (z_0(a_{0x}u + a_{0y}v))(\widetilde{Q}_1)d\tau\, d\omega$$
$$- \frac{1}{2\pi} \int_0^{2\pi} \int_{t_n}^{t_{n+1}} (z_0 S)(\widetilde{Q}_1)d\tau\, d\omega. \tag{2.11}$$

This is the exact integral representation for p. Integrating now (2.7) in time from t_n to t_{n+1} gives

$$\sin\omega(z_0 u)(P) - \sin\theta(z_0 u)(Q_2) - \int_{t_n}^{t_{n+1}} \left(\frac{d}{dt}(\sin\theta z_0)u\right)(\widetilde{Q}_2)d\tau - \cos\omega(z_0 v)(P) + \cos\theta(z_0 v)(Q_2)$$
$$- \int_{t_n}^{t_{n+1}} \left(\frac{d}{dt}(\cos\theta z_0)v\right)(\widetilde{Q}_2)d\tau + \int_{t_n}^{t_{n+1}} (a_0(\sin\theta p_x - \cos\theta p_y))(\widetilde{Q}_2)d\tau = 0. \tag{2.12}$$

Note that the first two integrals in (2.12) disappears due to the ray Eq. (2.5). Now, multiplying (2.12) by $\sin\omega$ and integrating over ω gives

$$\pi(z_0 u)(P) - \pi(z_0 u)(Q_2) + \pi a_0(Q_2) \int_{t_n}^{t_{n+1}} p_x(\widetilde{Q}_2)d\tau = 0. \tag{2.13}$$

Multiply (2.10) by $\cos\omega$ and integrate over ω to get

$$\pi z_0(P)u(P) = \int_0^{2\pi} (-p + z_0 u \cos\theta + z_0 v \sin\theta)(Q_1)\cos\omega\, d + \int_0^{2\pi} \int_{t_n}^{t_{n+1}} (z_0(a_{0x}u + a_{0y}v))(\widetilde{Q}_1)\cos\omega\, d\tau\, d\omega$$
$$+ \int_0^{2\pi} \int_{t_n}^{t_{n+1}} (z_0 S)(\widetilde{Q}_1)\cos\omega\, d\tau\, d\omega. \tag{2.14}$$

Adding (2.13) and (2.14) and rearranging yields

$$u(P) = \frac{1}{2\pi z_0(P)} \int_0^{2\pi} (-p + z_0 u \cos\theta + z_0 v \sin\theta)(Q_1)\cos\omega d\omega + \frac{1}{2\pi z_0(P)} \int_0^{2\pi} \int_{t_n}^{t_{n+1}} z_0(a_{0x}u + a_{0y}v)(\widetilde{Q}_1)\cos\omega\, d\tau\, d\omega$$
$$+ \frac{1}{2}u(Q_2) - \frac{1}{2\rho_0(P)} \int_{t_n}^{t_{n+1}} p_x(\widetilde{Q}_2)d\tau + \frac{1}{2\pi z_0(P)} \int_0^{2\pi} \int_{t_n}^{t_{n+1}} (z_0 S)(\widetilde{Q}_1)\cos\omega\, d\tau\, d\omega. \tag{2.15}$$

This is the exact integral representation of u. Analogously the exact integral representation for v can be derived

$$v(P) = \frac{1}{2\pi z_0(P)} \int_0^{2\pi} (-p + z_0 u \cos\theta + z_0 v \sin\theta)(Q_1)\sin\omega d\omega + \frac{1}{2\pi z_0(P)} \int_0^{2\pi} \int_{t_n}^{t_{n+1}} (z_0(a_{0x}u + a_{0y}v))(\widetilde{Q}_1)\sin\omega\, d\tau\, d\omega$$
$$+ \frac{1}{2}v(Q_2) - \frac{1}{2\rho_0(P)} \int_{t_n}^{t_{n+1}} p_y(\widetilde{Q}_2)d\tau + \frac{1}{2\pi z_0(P)} \int_0^{2\pi} \int_{t_n}^{t_{n+1}} (z_0 S)(\widetilde{Q}_1)\sin\omega\, d\tau\, d\omega. \tag{2.16}$$

In order to be consistent with our previous papers in what follows we put $Q \equiv Q_1$ and $Q_0 \equiv Q_2$.

Remark 2.1. Note that in [17,18,26] the exact evolution operator is derived in a slightly different way. It should be pointed out that the previous procedure will yield the same evolution operator as we have obtained here.

3. Approximate evolution operator

In this section we approximate the exact integral representation (2.11),(2.15) and (2.16) by suitable numerical quadratures and derive the corresponding approximate evolution operators.

Note that the exact integral equations contain time integrals involving the derivatives of the unknown variables. These are the terms that need our attention. First, let us consider in (2.15), (2.16) the integrals of p_x and p_y along a time like bicharacteristic. In order to eliminate these integrals we use the differential Eq. (1.3) and replace p_x and p_y. Integration of the second equation of (1.3) in time gives

$$\frac{1}{2}u(P) - \frac{1}{2}u(Q_0) = -\frac{1}{2\rho_0(P)} \int_{t_n}^{t_{n+1}} p_x(\widetilde{Q}_0)d\tau. \tag{3.1}$$

Thus, plugging (3.1) in (2.15) the integral containing p_x disappears. The integral of p_y in (2.16) is treated analogously. This yields the following equivalent formulation of the exact integral equations for u, v that is the base for the so-called EG1 approximate evolution operator, cf. [17]:

$$u(P) = \frac{1}{\pi z_0(P)} \int_0^{2\pi} (-p + z_0 u \cos\theta + z_0 v \sin\theta)(Q) \cos\omega \, \mathrm{d}\omega + \frac{1}{\pi z_0(P)} \int_0^{2\pi} \int_{t_n}^{t_{n+1}} z_0(a_{0x}u + a_{0y}v)(\widetilde{Q}) \cos\omega \, \mathrm{d}\tau \, \mathrm{d}\omega$$

$$+ \frac{1}{\pi z_0(P)} \int_0^{2\pi} \int_{t_n}^{t_{n+1}} (z_0 S)(\widetilde{Q}) \cos\omega \, \mathrm{d}\tau \, \mathrm{d}\omega \tag{3.2}$$

$$v(P) = \frac{1}{\pi z_0(P)} \int_0^{2\pi} (-p + z_0 u \cos\theta + z_0 v \sin\theta)(Q) \sin\omega \, \mathrm{d}\omega + \frac{1}{\pi z_0(P)} \int_0^{2\pi} \int_{t_n}^{t_{n+1}} (z_0(a_{0x}u + a_{0y}v))(\widetilde{Q}) \sin\omega \, \mathrm{d}\tau \, \mathrm{d}\omega$$

$$+ \frac{1}{\pi z_0(P)} \int_0^{2\pi} \int_{t_n}^{t_{n+1}} (z_0 S)(\widetilde{Q}) \sin\omega \, \mathrm{d}\tau \, \mathrm{d}\omega. \tag{3.3}$$

On the other hand, the integral representation (2.11), (2.15), (2.16) can still be used as a base for the approximate evolution operator. In the so-called EG3 framework the time integrals of p_x and p_y are first approximated by the rectangle rule at time $\tau = t_n$. The resulting terms at t_n are further approximated by an integral average along the wavefront. An application of the Gauss theorem then enables us to replace the derivatives, see [17]. In order to use the averages along wavefronts one requires the exact form of the wavefront. In the next section we will show that the wavefronts can be approximated by circles up to the second order accuracy. Using the approximate wavefront given in Section 3.1 the FVEG method based on the EG3 approximate evolution operator has been derived and implemented. However our numerical experiments indicate that the EG1 approximate evolution operator yields better accuracy than the application of the EG3 operator. In what follows we restrict therefore to the FVEG scheme using the EG1 approximate evolution operator.

Henceforth we assume $\Delta x = \mathcal{O}(\Delta t), \Delta y = \mathcal{O}(\Delta t)$ due to the CFL stability condition

$$\max\{\max_{x,y} a_0(x,y)\Delta t/\Delta x, \max_{x,y} a_0(x,y)\Delta t/\Delta y\} < \nu, \tag{3.4}$$

where $\nu \leqslant 1$ is the corresponding stability limit.

3.1. Approximation of the wavefront

As follows from (2.5) the geometry of the wavefront is described by the angle $\theta = \theta(t_n, \omega)$. In this section we will show that the wavefronts are circles up to second order accuracy. This allows us to evaluate spatial integrals in (2.11),(3.2) and (3.3) efficiently. The spatially varying wave speed, which determines the radius of these circles, offers two possibilities to approximate the wavefront: a single circle or arcs of circles that are related to the computational grid, see Fig. 3. Using our previous results from [18] we can evaluate for any polynomial function all spatial integrals along circles or arcs of circles exactly. This is a crucial step in the construction of the FVEG schemes. Indeed, we take all of the infinitely many directions of wave propagations explicitly into account. Moreover exact integration of piecewise polynomial approximate functions yields a very efficient numerical method, much more accurate then standard finite volume schemes [18], [20].

Let us note that if the wave speed a_0 is given by a linear function then the wavefronts are in fact circles. This can be shown analytically, see Appendix A. The centers of circles are then dependent on the gradient of a_0. This can be used in the vicinity of our bilinear reconstruction. On the other hand in order to keep the approximate evolution operator simple we can still use circles with center at Q_0. Our numerical experiments confirm that this yields a scheme which is at least twice faster while having similar accuracy. In fact, differences in the global errors were just marginal.

Since the independent variable of the integrals in (2.11),(3.2) and (3.3) is ω we are looking for an approximation of θ in terms of ω. The normal of the wavefront of the first bicharacteristic family is described by, cf. (2.5),

$$\frac{\mathrm{d}\theta}{\mathrm{d}t} = -a_{0x}\sin\theta + a_{0y}\cos\theta, \quad \theta(t_{n+1}) = \omega.$$
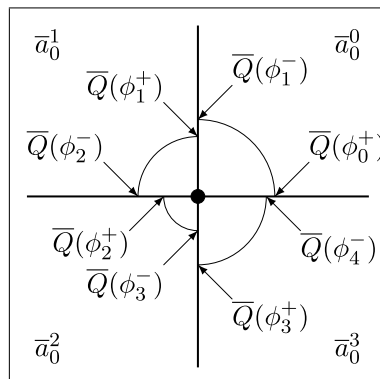

Fig. 3. Approximate wave front consisting of 4 arcs of circles; relative position of boundary terms and wave speeds for a vertex of computational grid.

Due to the CFL condition (3.4) the wavefront will never exceed one cell of the computational grid. Thus we can assume

$$a_0(x,y) = \bar{a}_0 + \mathcal{O}(\Delta x), \quad \bar{a}_{0_x}(x,y) = \bar{a}_{0_x} + \mathcal{O}(\Delta x), \quad \bar{a}_{0_y}(x,y) = \bar{a}_{0_y} + \mathcal{O}(\Delta x), \tag{3.5}$$

where $\bar{a}_0, \bar{a}_{0_x}, \bar{a}_{0_y}$ are arbitrary but fixed first order approximations of the wave speed and its derivatives at $(x(t_{n+1}), y(t_{n+1})); x = x(t_{n+1}) + \mathcal{O}(\Delta x), y = y(t_{n+1}) + \mathcal{O}(\Delta x)$. This implies

$$\begin{aligned}
\theta(t_n) &= \theta(t_{n+1}) + \frac{d\theta}{dt}\bigg|_{t=t_{n+1}} (t_n - t_{n+1}) + \mathcal{O}(\Delta t^2) \\
&= \omega - [-\bar{a}_{0_x}\sin\omega + \bar{a}_{0_y}\cos\omega]\Delta t + \mathcal{O}(\Delta t^2) \tag{3.6} \\
&= \omega + \mathcal{O}(\Delta t). \tag{3.7}
\end{aligned}$$

The ray equation for the x-component of the first bicharacteristic family reads

$$\frac{dx}{dt} = -a_0(x,y)\cos\theta.$$

Using (3.5) and (3.7) we obtain

$$\frac{dx}{dt} = -\bar{a}_0\cos\omega + \mathcal{O}(\Delta t).$$

Assuming without loss of generality $x(t_{n+1}) = 0$ and integrating in time from t_{n+1} to t_n yield

$$x(t_n, \omega) = \bar{a}_0\Delta t\cos\omega + \mathcal{O}(\Delta t^2).$$

The expression for y-component is derived similarly. The approximations for x and y are fundamental for further derivations. They indeed give the opportunity to approximate the wavefront by circles centered at $(x(t_{n+1}), y(t_{n+1}))$ and parameterized by ω

$$Q(x,y,t_n) = \begin{pmatrix} x(t_n,\omega) \\ y(t_n,\omega) \end{pmatrix} = \bar{a}_0\Delta t \begin{pmatrix} \cos\omega \\ \sin\omega \end{pmatrix} + \mathcal{O}(\Delta t^2) \begin{pmatrix} 1 \\ 1 \end{pmatrix}. \tag{3.8}$$

Let $f \in C^1$ be any function to be evaluated on the wavefront then by the Taylor expansion

$$f(Q) = f(\bar{a}_0\Delta t\cos\omega, \bar{a}_0\Delta t\sin\omega) + \mathcal{O}(\Delta t^2). \tag{3.9}$$

This leads us to the following definition of the approximate wavefront:

$$\{\overline{Q} := (\bar{a}_0\Delta t\cos\omega, \bar{a}_0\Delta t\sin\omega)^T, \quad \omega \in [0, 2\pi]\}. \tag{3.10}$$

As we have already pointed out $\bar{a}_0$ might be defined such that

$$\bar{a}_0 = \bar{a}_0(\omega), \quad \bar{a}_{0_x} = \bar{a}_{0_x}(\omega), \quad \bar{a}_{0_y} = \bar{a}_{0_y}(\omega), \quad \omega \in [0, 2\pi]. \tag{3.11}$$

The dependency on ω gives the opportunity to approximate the wavefront by parts of circles according to the computational grid. For example, if the point $P = (x(t_{n+1}), y(t_{n+1}))$ is a vertex of the computational grid consisting of rectangles, the wavefront can be created by four different arcs of circles, cf. Fig. 3.

3.2. Approximations of the exact integral representation

Let us first approximate the following mantle integral:

$$\int_0^{2\pi} \int_{t_n}^{t_{n+1}} z_0(a_{0x}u + a_{0y}v)(\widetilde{Q})f(\omega) \, d\tau \, d\omega \tag{3.12}$$

that appears in (2.11), (3.2) and (3.3) with $f(\omega) = 1, f(\omega) = \cos\omega$ and $f(\omega) = \sin\omega$, respectively. Applying the rectangle rule at $\tau = t_n$ for time integration gives the $\mathcal{O}(\Delta t^2)$ error at one time step. The exact wavefront is then replaced by the approximate wavefront (3.10) and θ is approximated by (3.7). The wave speed a_0 and its spatial derivatives are approximated by (3.5), where $\bar{a}_0, \bar{a}_{0_x}, \bar{a}_{0_y}$ can be taken from the corresponding bilinear recovery. This yields the first order approximation. Note however that in the mantle integrals the first order terms are further multiplied by Δt that arises from the time integration. This gives the desired second order accuracy.

For the integrals involving the multi-dimensional source term S, cf. (2.9), and for the integrals along the bottom of cone a special treatment will be required.

3.2.1. Integrals involving the multi-dimensional source term S

In order to eliminate spatial derivatives in the multi-dimensional source term S the so-called useful lemma, cf. [17], is used. In the case of spatially dependent wave speed the wavefront might be approximated by arcs of circles and the integration by parts gives additional boundary terms.

Lemma 3.1. *Extended useful lemma*

Let $w \in C^1(\mathbb{R}^2), p \in C^1(\mathbb{R}), C = (a \cos \omega, a \sin \omega), \ a \in \mathbb{R}, \ \phi_1 \in [0, 2\pi], \ \phi_2 \in [0, 2\pi]$. *Then*

$$\int_{\phi_1}^{\phi_2} p(\omega)[w_x(C) \sin \omega - w_y(C) \cos \omega] \mathrm{d}\omega = \frac{1}{a} \left(\int_{\phi_1}^{\phi_2} p'(\omega) w(C) \mathrm{d}\omega + p(\phi_1) w(C(\phi_1)) - p(\phi_2) w(C(\phi_2)) \right).$$

Proof. Apply integration by parts, cf. [17], and take boundary terms into account. $\quad\square$

From [30] we note that the multi-dimensional source term S contains tangential derivatives of u and v for any curve with unit normal $(\cos \theta, \sin \theta)$ and hence extended useful lemma holds not only for the case when the wavefront consists of parts of circles but even for arbitrary curves. Let us point out that even if the wavefront is represented by a single circle the boundary terms occur due to discontinuities of the numerical approximation. These small jump terms might be neglected since the approximations converge. All numerical tests presented in the Section 5 indicate that if the boundary terms are included results are slightly more accurate. In fact, if the boundary terms are included the computational costs increase mostly at 10%. The global error is improved typically at the second nonzero digit.

Since $z_0 = \frac{\gamma p_0}{a_0}$ we have $z_0 S = \gamma p_0 (S/a_0)$, note that γp_0 is a constant and S contains a factor a_0. Applying the rectangle rule in time for the mantle integral involving S in (2.11) yields

$$I_1 := \int_0^{2\pi} \int_{t_n}^{t_{n+1}} \left(\frac{S}{a_0} \right) (\widetilde{Q}) \mathrm{d}\tau \mathrm{d}\omega = \Delta t \int_0^{2\pi} \left(\frac{S}{a_0} \right) (Q) \mathrm{d}\omega + \mathcal{O}(\Delta t^2).$$

Note that here Q is still a function of $\theta = \theta(t_n, \omega)$. Applying the first order approximation of θ (3.7), the approximate wavefront (3.10) and (3.9) yields

$$I_1 = \int_0^{2\pi} (u_x \sin^2 \omega - (u_y + v_x) \cos \omega \sin \omega + v_y \cos^2 \omega)(\overline{Q}) \mathrm{d}\omega + \mathcal{O}(\Delta t^2).$$

Let us consider a vertex of a computational grid consisting of rectangles, cf. Section 4. We want to predict a solution at this vertex. The approximate wavefront is then divided into four slices whose boundaries can be symbolized by the angles $\phi_j = j\pi/2$ for $j = 0, 1, \ldots, 4$. We define for any function f and angle ϕ, cf. Fig. 3,

$$f(\overline{Q}(\phi^-)) := \lim_{\tilde{\phi} \to \phi^-} f(\overline{Q}(\tilde{\phi})), \quad f(\overline{Q}(\phi^+)) := \lim_{\tilde{\phi} \to \phi^+} f(\overline{Q}(\tilde{\phi})).$$

Due to (3.11) different choices of $\bar{a}_0$ according to the cells neighboring the vertex are possible. We will express this in the next formulae by $\bar{a}_0^j, j = 0, \ldots, 3$. Application of Lemma 3.1 gives

$$I_1 = \sum_{\substack{j=0 \\ \phi_j = j\pi/2}}^3 \frac{1}{\bar{a}_0^j} \left(\int_{\phi_j}^{\phi_{j+1}} (u \cos \omega + v \sin \omega)(\overline{Q}) \mathrm{d}\omega \right) + \sum_{\substack{j=0 \\ \phi_j = j\pi/2}}^3 \frac{1}{\bar{a}_0^j} [(u \sin \phi_j - v \cos \phi_j)(\overline{Q}(\phi_j^+)) - (u \sin \phi_{j+1}$$

$$- v \cos \phi_{j+1})(\overline{Q}(\phi_{j+1}^-))] + \mathcal{O}(\Delta t^2). \tag{3.13}$$

Note that the first sum of integrals on the right hand side can be written equivalently as

$$\int_0^{2\pi} \frac{1}{\bar{a}_0} (u \cos \omega + v \sin \omega)(\overline{Q}) \mathrm{d}\omega,$$

where $\bar{a}_0 = \bar{a}_0(\omega)$ or $\bar{a}_0 = \text{const}$. The mantle integrals involving the multi-dimensional source term S in (3.2), (3.3) are approximated in an analogous way.

3.2.2. Integrals along the bottom of cone

Since in the integrals along the bottom of cone there is no extra factor Δt arising from the time integration we need to approximate θ in terms of ω up to second order. Let us consider

$$I_2 := \int_0^{2\pi} (z_0(u \cos \theta + v \sin \theta))(Q) f(\omega) \mathrm{d}\omega,$$

that appears in (2.11), (3.2), (3.3) with $f(\omega) = 1, f(\omega) = \cos \omega$ and $f(\omega) = \sin \omega$, respectively. Using (3.6), the Taylor expansion of trigonometric functions and (3.9) lead to

$$I_2 = \int_0^{2\pi} (z_0(u \cos \omega + v \sin \omega))(\overline{Q}) f(\omega) \mathrm{d}\omega + \Delta t \int_0^{2\pi} (z_0[u \sin \omega - v \cos \omega][-\bar{a}_{0_x} \sin \omega + \bar{a}_{0_y} \cos \omega])(\overline{Q}) f(\omega) \mathrm{d}\omega + \mathcal{O}(\Delta t^2),$$

$$\tag{3.14}$$

that is the desired second order approximation.

3.2.3. The approximate evolution operator

Applying the rectangle rule in time and the approximations (3.13), (3.14) to the exact integral representation (2.11),(3.2), (3.3) we obtain the following approximate evolution operator for the wave equation system with variable wave speed:

$$
\begin{aligned}
p(P) = \frac{1}{2\pi} \Bigg[& \int_0^{2\pi} (p - z_0(u\cos\omega + v\sin\omega))(\overline{Q})\mathrm{d}\omega \\
& - \Delta t \int_0^{2\pi} (z_0[u\sin\omega - v\cos\omega][-\bar{a}_{0_x}\sin\omega + \bar{a}_{0_y}\cos\omega])(\overline{Q})\mathrm{d}\omega - \Delta t \int_0^{2\pi} (z_0(\bar{a}_{0_x}u + \bar{a}_{0_y}v))(\overline{Q})\mathrm{d}\omega \\
& - \gamma p_0 \sum_{\substack{j=0 \\ \phi_j = j\pi/2}}^{3} \frac{1}{\bar{a}_0^j} \Bigg[\int_{\phi_j}^{\phi_{j+1}} (u\cos\omega + v\sin\omega)(\overline{Q})\mathrm{d}\omega + (u\sin\phi_j - v\cos\phi_j)(\overline{Q}(\phi_j^+)) \\
& - (u\sin\phi_{j+1} - v\cos\phi_{j+1})(\overline{Q}(\phi_{j+1}^-)) \Bigg] \Bigg] + \mathcal{O}(\Delta t^2),
\end{aligned}
$$

$$
\begin{aligned}
u(P) = \frac{1}{\pi z_0(P)} \Bigg[& \int_0^{2\pi} (-p + z_0(u\cos\omega + v\sin\omega))(\overline{Q})\cos\omega\,\mathrm{d}\omega \\
& + \Delta t \int_0^{2\pi} (z_0[u\sin\omega - v\cos\omega][-\bar{a}_{0_x}\sin\omega + \bar{a}_{0_y}\cos\omega])(\overline{Q})\cos(\omega)\mathrm{d}\omega \\
& + \Delta t \int_0^{2\pi} (z_0(\bar{a}_{0_x}u + \bar{a}_{0_y}v))(\overline{Q})\cos\omega\,\mathrm{d}\omega \\
& + \gamma p_0 \sum_{\substack{j=0 \\ \phi_j = j\pi/2}}^{3} \frac{1}{\bar{a}_0^j} \Bigg[\int_{\phi_j}^{\phi_{j+1}} (u(2\cos^2\omega - 1) + 2v\cos\omega\sin\omega)(\overline{Q})\mathrm{d}\omega \\
& + (u\cos\phi_j\sin\phi_j - v\cos^2\phi_j)(\overline{Q}(\phi_j^+)) \\
& - (u(\cos\phi_{j+1}\sin\phi_{j+1}) - v\cos^2\phi_{j+1})(\overline{Q}(\phi_{j+1}^-)) \Bigg] \Bigg] + \mathcal{O}(\Delta t^2),
\end{aligned}
$$

$$
\begin{aligned}
v(P) = \frac{1}{\pi z_0(P)} \Bigg[& \int_0^{2\pi} (-p + z_0(u\cos\omega + v\sin\omega))(\overline{Q})\sin\omega\,\mathrm{d}\omega \\
& + \Delta t \int_0^{2\pi} (z_0[u\sin\omega - v\cos\omega][-\bar{a}_{0_x}\sin\omega + \bar{a}_{0_y}\cos\omega])(\overline{Q})\sin(\omega)\mathrm{d}\omega \\
& + \Delta t \int_0^{2\pi} (z_0(\bar{a}_{0_x}u + \bar{a}_{0_y}v))(\overline{Q})\sin\omega\,\mathrm{d}\omega \\
& + \gamma p_0 \sum_{\substack{j=0 \\ \phi_j = j\pi/2}}^{3} \frac{1}{\bar{a}_0^j} \Bigg[\int_{\phi_j}^{\phi_{j+1}} (2u\cos\omega\sin\omega + v(2\sin^2\omega - 1))(\overline{Q})\mathrm{d}\omega \\
& + (u\sin^2\phi_j - v\cos\phi_j\sin\phi_j)(\overline{Q}(\phi_j^+)) \\
& - (u(\sin^2\phi_{j+1}) - v\cos\phi_{j+1}\sin\phi_{j+1})(\overline{Q}(\phi_{j+1}^-)) \Bigg] \Bigg] + \mathcal{O}(\Delta t^2).
\end{aligned}
$$

Note that if a_0 is constant then $\gamma p_0/a_0 = z_0$ is constant as well. In this case the approximate evolution operator proposed here coincides with the approximate evolution operator EG1 given in [17] if the jump boundary terms at $\overline{Q}(\phi_j^+)$ and $\overline{Q}(\phi_{j+1}^-)$ are omitted.

4. Finite volume evolution Galerkin method

Let us divide a computational domain Ω into a finite number of regular finite volumes $\Omega_{ij} := [i\Delta x, (i+1)\Delta x] \times [j\Delta y, (j+1)\Delta y]$ for $i = 0, \ldots, M, j = 0, \ldots, N; \Delta x, \Delta y$ are the mesh steps in x- and y-directions, respectively. Denote by $\boldsymbol{U}_{ij}^n$ the piecewise constant approximate solution on a mesh cell Ω_{ij} at time t_n and start with initial approximations obtained by the integral averages $\boldsymbol{U}_{ij}^0 = \frac{1}{|\Omega_{ij}|} \int_{\Omega_{ij}} \boldsymbol{U}(\cdot, 0)$. Integrating the conservation law (1.2) and applying the Gauss theorem on any mesh cell Ω_{ij} yield the following update formula for the finite volume evolution Galerkin scheme:

$$
\boldsymbol{U}_{ij}^{n+1} = \boldsymbol{U}_{ij}^n - \frac{\Delta t}{\Delta x}\delta_x^{ij}\bar{f}_1^{n+1/2} - \frac{\Delta t}{\Delta y}\delta_y^{ij}\bar{f}_2^{n+1/2}. \tag{4.1}
$$

Here $\delta_x^{ij}, \delta_y^{ij}$ stand for the central difference operators in x or y-direction and $\bar{f}_k^{n+1/2}, k = 1, 2$, represents an approximation to the cell interface flux at the intermediate time level $t^n + \Delta t/2$. We evolve the cell interface fluxes $\bar{f}_k^{n+1/2}$ to $t_n + 1/2$ using the approximate evolution operator denoted by $E_{\Delta t/2}$ and average them along the cell interface $\mathcal{E}$

$$\bar{f}_k^{n+1/2} := \sum_j \omega_j f_k(E_{\Delta t/2} \boldsymbol{U}^n(\boldsymbol{x}^j(\mathscr{E}))), \quad k = 1, 2. \tag{4.2}$$

Here $\boldsymbol{x}^j(\mathscr{E})$ are the nodes and ω_j the weights of the quadrature for the flux integration along the edges.

4.1. Staggered grid

In order to evaluate cell interface fluxes $\bar{f}_k^{n+1/2}$, $k = 1, 2$, we need to approximate spatially varying a_0 and z_0. The most natural approach is to use the cell averages $\bar{a}_{0_{ij}} = \frac{1}{|\Omega_{ij}|} \int_{\Omega_{ij}} a_0$ and $\bar{z}_{0_{ij}} = \frac{1}{|\Omega_{ij}|} \int_{\Omega_{ij}} z_0$. In this case a_0 and z_0 are approximated on the
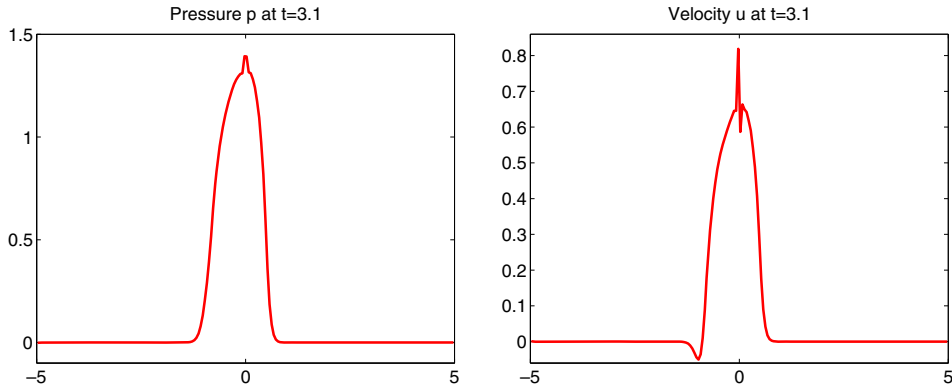
Fig. 4. Flawed solution without staggered grid approximation for the wave speed and impedance.
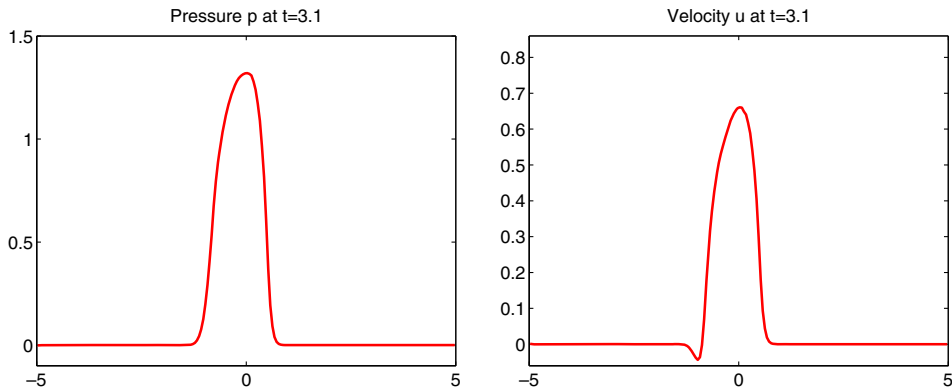

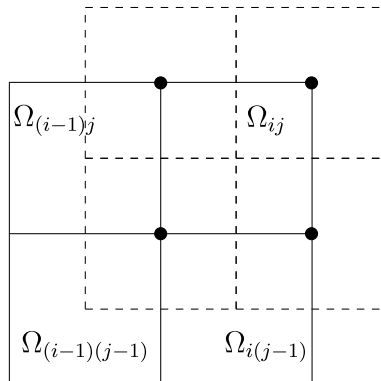**Fig. 5.** Solution with staggered grid approximation for the wave speed and impedance.

Fig. 6. Staggered grid and quadrature nodes.

same grid as conservative variables and they are discontinuous along cell interfaces. In what follows we will show that this approach leads to artificial kinks at interfaces.

In order to illustrate the above phenomena let us consider the following example, cf. [13]. Set $\gamma = 1 = p_0$. The wave speed is:

$$a_0(x) := \begin{cases} 1.0 & \text{if} \quad x < 0 \\ 0.5 & \text{if} \quad x \geqslant 0, \end{cases}$$

initial pressure and velocity read

$$p(x) = u(x) = \begin{cases} \sqrt{1 - (x + 3)^2} & \text{if} \ -4 < x < -2, \\ 0 & \text{otherwise}. \end{cases}$$

The computational domain is the interval $[-5; 5]$. Absorbing boundary conditions have been implemented by extrapolating all variables. We set the end time to $t = 3.1$ and use a mesh with 200 cells. In the second order FVEG method the minmod

Table 1
Data for the one-dimensional test cases.

	Example 1	Example 2	Example 3
Isentropic exponent γ	1.4	$\sqrt{3}$	1.4
Background pressure p_0	1.0	0.5	$320/119 \approx 2.69$
Wave speed a_0	$1 + \frac{1}{2}\cos(4\pi x)$	$1 + \frac{1}{2}\sin(10\pi x)$	0.6 if $0.35 < x < 0.65$ 2.0 otherwise
Initial pressure p	$\sin(2\pi x)$	$1.75 - 0.75\cos(10\pi x - 4\pi)$ 1.0	if $0.4 < x < 0.6$ otherwise
Final time	$t = 1.0$	$t = 0.3$	
Computational domain	$\Omega = [0; 1]$		
Boundary condition	Periodic		
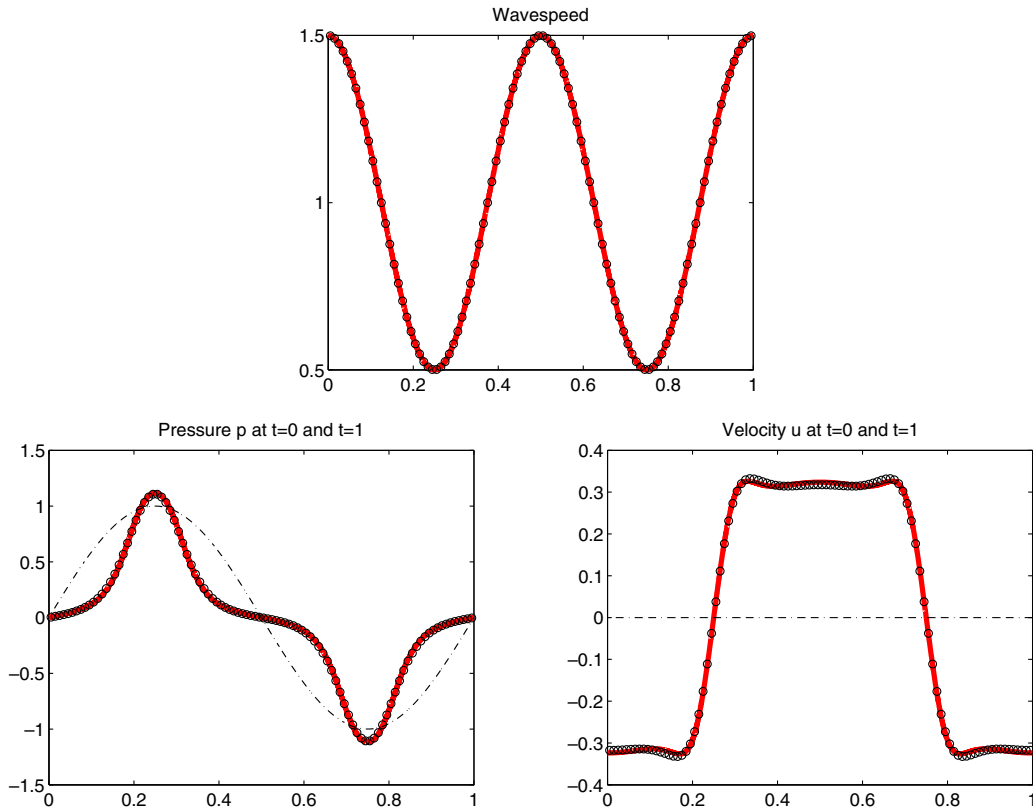
Fig. 7. Example 1 with a smooth wave speed.

limiter was used in order to limit overshoots and undershoots of linearly recovered approximations. In Fig. 4 both components of the solution at time $t = 3.1$ are depicted. We can clearly recognize artificial overshoots as the wave runs through the interface at $x = 0$.

This effects can be explained by the following analysis. Let us reconsider the evolution Galerkin operator simplified to first order and apply it on a one-dimensional x-dependent data. Assume that derivatives of u are bounded and omit all $\mathcal{O}(\Delta t)$ terms

$$p(P) = \frac{1}{2\pi} \int_0^{2\pi} (p - z_0 u \cos \omega)(\overline{Q}) \mathrm{d}\omega + \mathcal{O}(\Delta t)$$

$$u(P) = \frac{1}{\pi z_0(P)} \int_0^{2\pi} (-p + z_0 u \cos \omega)(\overline{Q}) \cos \omega \mathrm{d}\omega + \mathcal{O}(\Delta t).$$

It is easy to realize that the term $z_0 u$ yields difficulties. Using piecewise constant approximation and predicting $p(P)$ at cell interface we obtain

$$\frac{1}{2\pi} \int_0^{2\pi} (z_0 u)(\overline{Q}) \cos \omega \mathrm{d}\omega = \frac{1}{\pi} \Big(\frac{z_{0r} + z_{0l}}{2} (u_r - u_l) + (z_{0r} - z_{0l}) \frac{u_r + u_l}{2} \Big).$$

It is the discontinuity of impedance z_0 along the integration path that yields a jump term. In order to achieve continuous approximation of z_0 we can replace z_{0l} and z_{0r} by their average $(z_{0l} + z_{0r})/2$. Choosing such an approximation the jump term disappears and the artificial kinks vanish in numerical experiments as demonstrated in plots of Fig. 5.

The above example clearly indicates that the discontinuous approximation of z_0 along an integration path has to be avoided. To overcome the above problem we introduce the so-called staggered grid $\{\widetilde{\Omega}_{kl}\}_{k,l}$, where $\widetilde{\Omega}_{kl} := [(k-1)\Delta x/2, (k+1)\Delta x/2] \times [(l-1)\Delta y/2, (l+1)\Delta y/2]$ for $k = 0, \ldots, M$, $l = 0, \ldots, N$. The staggered grid will be used in the predictor (evolution) step in order to approximate the wave speed a_0 and the impedance z_0.

For the flux integration along cell interfaces in (4.2) the trapezoidal rule has been used. Thus, the quadrature nodes are the vertices of computational cells and each cell $\widetilde{\Omega}_{kl}$ of the staggered grid is associated to the corresponding quadrature node, see Fig. 6. Note that the use of midpoint rule would reduce the FVEG method to a standard dimensional splitting Godunov-type scheme. It should be pointed out that we can still approximate the wave front by one circle or by arcs of circles, cf. (3.11). Our numerical experiments indicate only marginal differences between these two approximations. In what follows we represent for simplicity the wave front by a single circle. Now, along the whole integration path continuous approximation of a_0 and z_0 on $\widetilde{\Omega}_{kl}$ is used and no spurious oscillations develop.
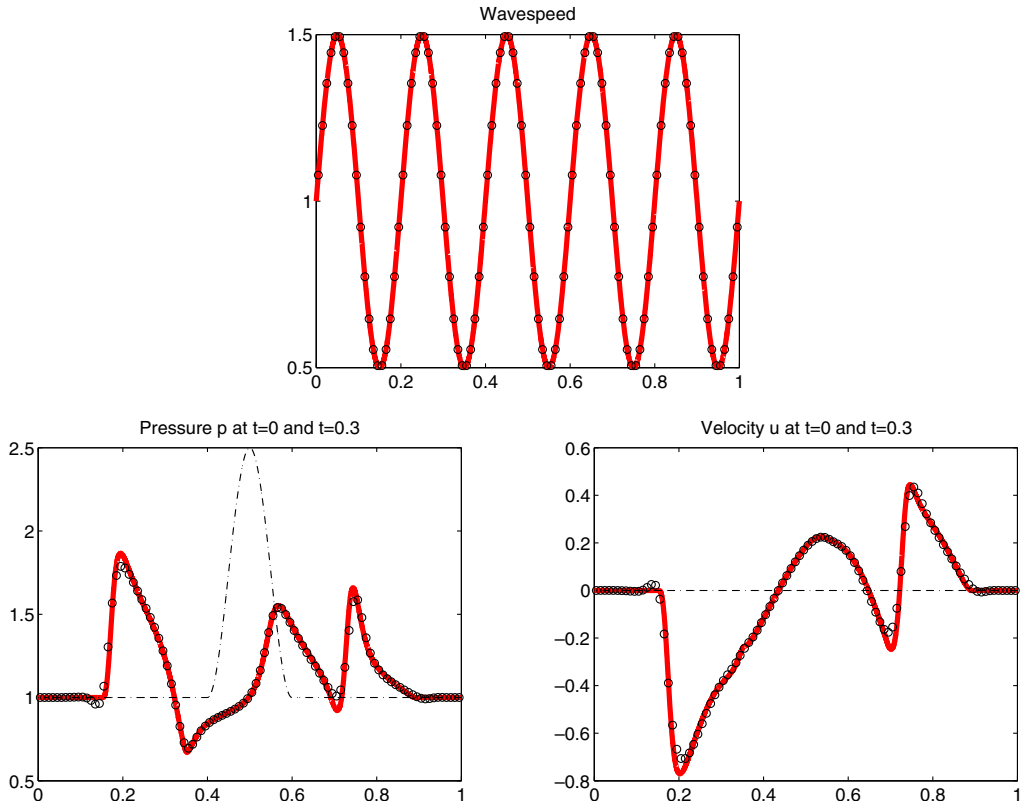

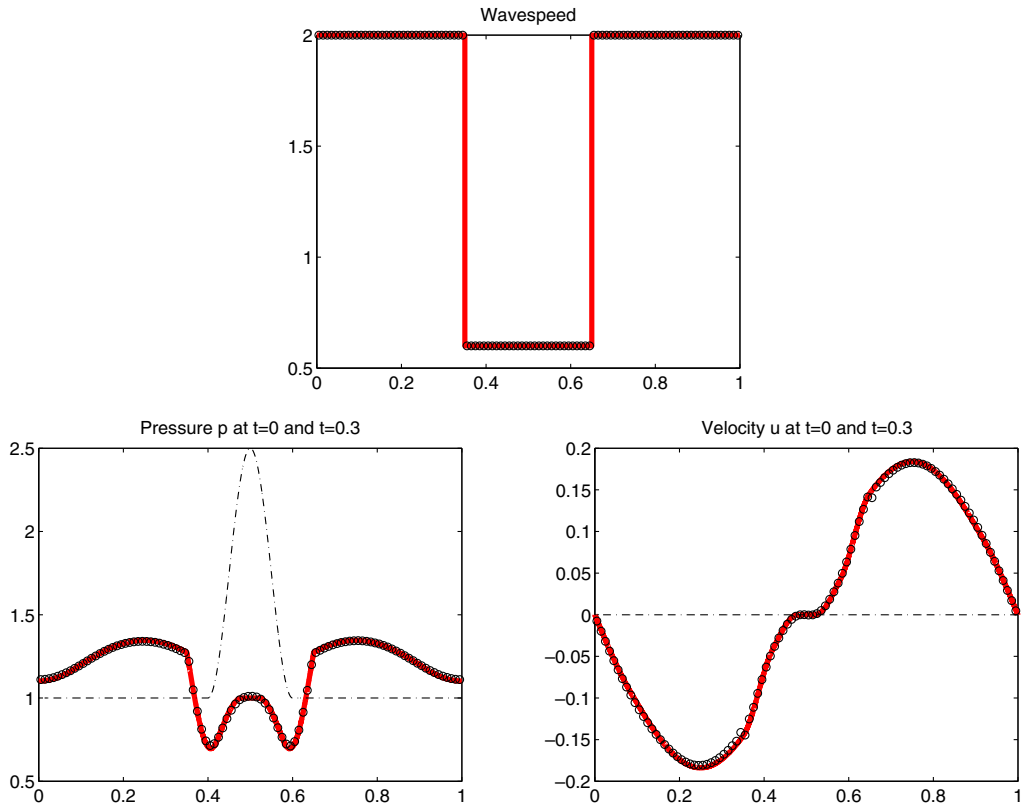**Fig. 8.** Example 2 with nonsmooth initial pressure.

Fig. 9. Example 3 with a discontinuous wave speed.

Table 2
L^1 errors and experimental order of convergence; Example 1 with a smooth wave speed, reference solution: 409 600 cells.

N	L^1 error of p	EOC	L^1 error of u	EOC	L^1 error of $\rho_0 u$	EOC
25	7.65e−02		4.53e-02		8.80e−02	
50	2.60e−02	1.557	1.46e−02	1.633	2.82e−02	1.642
100	5.87e−03	2.146	4.30e−03	1.763	7.23e−03	1.962
200	1.41e−03	2.053	9.60e−04	2.164	1.65e−03	2.134
400	3.40e−04	2.056	2.23e−04	2.107	3.93e−04	2.065
800	8.39e−05	2.017	5.40e−05	2.044	9.75e−05	2.012
1600	2.09e−05	2.005	1.33e−05	2.018	2.44e−05	2.000
3200	5.22e−06	2.001	3.31e−06	2.008	6.09e−06	1.998
6400	1.30e−06	2.000	8.25e−07	2.004	1.52e−06	1.999
12 800	3.26e−07	2.001	2.06e−07	2.002	3.81e−07	2.000

Table 3
L^1 errors and experimental order of convergence; Example 2, reference solution: 409 600 cells.

N	L^1 error of p	EOC	L^1 error of u	EOC	L^1 error of $\rho_0 u$	EOC
25	7.66e−02		8.80e−02		9.19e−02	
50	3.74e−02	1.033	3.22e−02	1.448	4.52e−02	1.023
100	1.41e−02	1.406	1.19e−02	1.442	1.91e−02	1.240
200	3.81e−03	1.891	2.99e−03	1.988	5.54e−03	1.788
400	8.93e−04	2.092	7.47e−04	1.999	1.34e−03	2.043
800	2.16e−04	2.049	1.94e−04	1.944	3.27e−04	2.038
1600	5.41e−05	1.995	5.05e−05	1.943	8.20e−05	1.994
3200	1.37e−05	1.985	1.30e−05	1.960	2.07e−05	1.986
6400	3.45e−06	1.986	3.30e−06	1.974	5.22e−06	1.986
12 800	8.72e−07	1.983	8.39e−07	1.977	1.32e−06	1.985

In order to obtain the second order scheme a recovery procedure has to be applied. The solution components p, u and v are recovered using usual bilinear recovery, cf. [18]. Analogously, the wave speed a_0 and the impedance z_0 are recovered on the staggered grid. The slopes are limited by a suitable limiter at each time step. In our numerical experiments we worked with the minmod and the monotonized minmod limiters, cf. [13].

We should point out that the use of staggered grid approach in order to model spatially varying wave speeds is a novel feature of the FVEG method developed in this paper.

5. Numerical experiments

In this chapter we illustrate behaviour of the new FVEG method on a set of one- and two-dimensional experiments with continuous as well as discontinuous wave speeds. All experiments have been done with two-dimensional FVEG method. In the case of one-dimensional experiments we have imposed zero velocity $v = 0$ and use simply the midpoint rule for the flux integration along cell interfaces. In all our experiments we have set the CFL number $v = 0.55$ which is in agreement with our previous theoretical stability analysis [22]. Since the main aim of this section is to test accuracy and robustness of the newly developed FVEG scheme, we confine ourselves to test problems with simple boundary conditions, e.g. periodic or extrapolation boundary conditions. The reader is referred to [21] for more detailed study on various techniques for implementation of reflected and absorbing boundary conditions in the framework of the evolution Galerkin scheme.

5.1. One-dimensional experiments

The first experiment is motivated by [17], the other two one-dimensional tests are motivated by [1]. In all test cases the initial velocities u and v are set to zero. Data setting for the corresponding experiments are given in Table 1. All results of the one-dimensional experiments presented in Figs. 7–9 are computed on a mesh with 100 cells, the reference solutions have been computed on a mesh with 25 600 cells. The dashed line plots are the initial conditions. The results have been also used for the evaluation of the experimental order of convergence (EOC) and no slope limiter has been applied here.
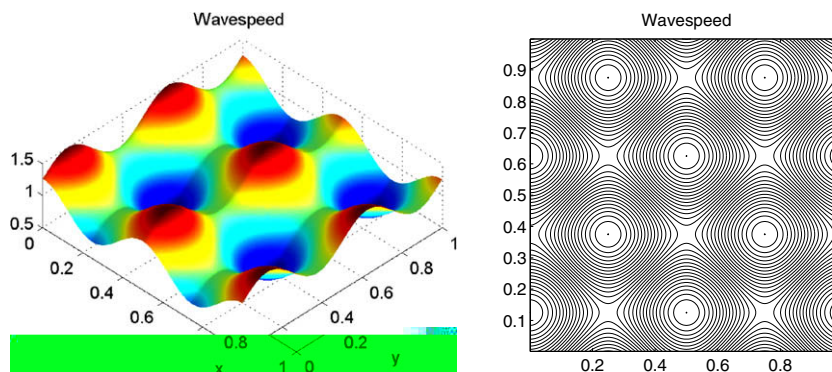
5.1.1. Example 1: smooth data

In this experiment we study behaviour of the scheme for smoothly varying wave speed, cf. Fig. 7. We can notice that even on a mesh with 100 cells all qualitative properties of the solution are well resolved. Table 2 demonstrates the second order accuracy of the FVEG scheme using bilinear recovery.

Table 4
L^1 errors and experimental order of convergence; Example 3 with a discontinuous wave speed, reference solution: 409 600 cells.

N	L^1 error of p	EOC	L^1 error of u	EOC	L^1 error of $\rho_0 u$	EOC
25	1.03e−01		2.12e−02		7.99e−02	
50	4.08e−02	1.334	1.51e−02	0.484	6.81e−02	0.230
100	5.36e−03	2.928	1.94e−03	2.965	5.78e−03	3.558
200	1.24e−03	2.108	4.88e−04	1.987	1.89e−03	1.610
400	3.15e−04	1.981	1.20e−04	2.023	5.13e−04	1.883
800	9.40e−05	1.743	3.11e−05	1.948	1.53e−04	1.741
1600	2.06e−05	2.192	7.48e−06	2.056	3.42e−05	2.166
3200	6.04e−06	1.768	1.95e−06	1.938	1.00e−05	1.773
6400	1.33e−06	2.182	4.72e−07	2.047	2.19e−06	2.187
12 800	2.87e−07	2.210	9.90e−08	2.253	4.54e−07	2.272

Fig. 10. Example 5.2.1, graph and isolines of spatially varying wave speed a_0.

Pressure p at time t = 0
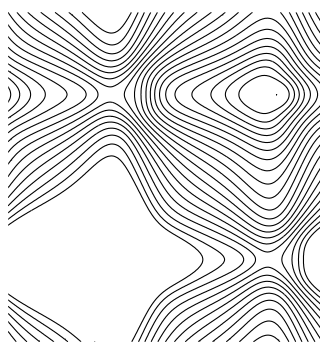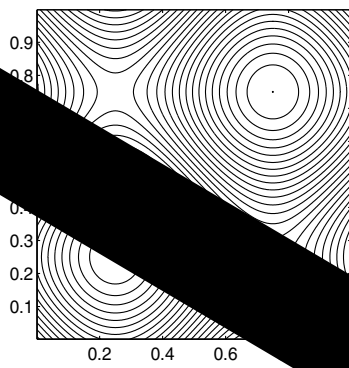
5.1.2. Examples 2 and 3: nonsmooth data

These experiments are motivated by LeVeque [1]. Note that in [1] $p_0 \neq$ const. and thus our results can not be directly compared with those presented by LeVeque et al. We therefore calculated γ and p_0 such that the average of the impedance used here and the average of the impedance used in [1] coincide.

Note that the initial condition of pressure in Examples 2 and 3 is only C^1, not C^2 as we assumed in the derivations using the local truncation analysis. Numerical experiments still indicate that the scheme is second order accurate, cf. Table 3. In the Example 3 there is an additional difficulty as the wave speed is discontinuous. The reconstruction of the wave speed is always set to constant function, as otherwise a slope of $\mathcal{O}(1/\Delta x)$ will be created at the discontinuity. Note that no slope limiter has been used here due to the EOC measurements.

Interestingly, the EOC values in Table 4 seem to oscillate in some sense. This can be explained in the following way. The values for z_0 and a_0 on the staggered grid are automatically created by our implementation. This procedure uses midpoint rule for approximation of the cell averages. One can show that then for different resolutions a numerical discontinuity can be right to or left to the analytical discontinuity. This is true for both discontinuities of the wave speed. Furthermore, the left and right discontinuities are in this sense independent from each other. We believe that this is the source of the described behaviour in the Table 4. Since the implementation handles the situation fully automatically and the EOCs are overall close to second order, this is in fact advantageous, because there is no need of a special treatment of the wave speed in such a situation.

We can notice in Fig. 9 that there is a small kink in the velocity field at the discontinuity of the wave speed. Even if one apply a minmod limiter this kink still remains there but vanishes as the mesh is refined.

5.2. Two-dimensional experiments

All numerical experiments presented in Figs. 10–15 are computed on a mesh with 400×400 cells. The two-dimensional tests confirm the expected second order accuracy and show good resolution, especially in the radially symmetric test case. This confirms the reliability and robustness of truly multi-dimensional FVEG scheme.

5.2.1. Wave propagation in a medium with smoothly varying wave speed

Motivated by [17] we tested truly two-dimensional wave propagation in a medium with smoothly varying wave speed. Set $\gamma = 1.4$ and $p_0 = 1.0$. The wave speed and the initial pressure are given by

$$a_0(x,y) = 1 + \frac{1}{4}(\sin(4\pi x) + \cos(4\pi y)),$$
$$p(x,y) = \sin(2\pi x) + \cos(2\pi y),$$

respectively, see Fig. 10 for the graph of waves speed. The initial velocities u and v are set to zero. The computational domain is $[0;1] \times [0;1]$ with periodic boundary conditions and the final time is set to $t = 1.0$.

In Fig. 11 the graphs and isolines of the initial pressure and all components of the final solution are depicted.

Furthermore, in order to demonstrate good approximation properties of the newly developed FVEG method we compare the L^1 errors with those obtained by some standard second order method. In particular, we have chosen the Lax-Wendroff finite difference method (rotated Richtmyer version), see, e.g., [25]. For completeness, let us recall that the Lax-Wendroff scheme can be also formulated as a predictor–corrector method in the following way:

$$\boldsymbol{U}_{i+1/2,j+1/2}^{n+1/2} = \left[\mu_x \mu_y \boldsymbol{U} - \frac{1}{2} \left(\frac{\Delta t}{\Delta x} \mu_y \delta_x \boldsymbol{f}_1 + \frac{\Delta t}{\Delta y} \mu_x \delta_y \boldsymbol{f}_2 \right) \right]_{i+1/2,j+1/2}^{n},$$
$$\boldsymbol{U}_{i,j}^{n+1} = \boldsymbol{U}_{i,j}^{n} - \left[\frac{\Delta t}{\Delta x} \mu_y \delta_x \boldsymbol{f}_1 + \frac{\Delta t}{\Delta y} \mu_x \delta_y \boldsymbol{f}_2 \right]_{i,j}^{n+1/2}.$$

Here μ denotes an averaging operator and δ a standard central difference operator.
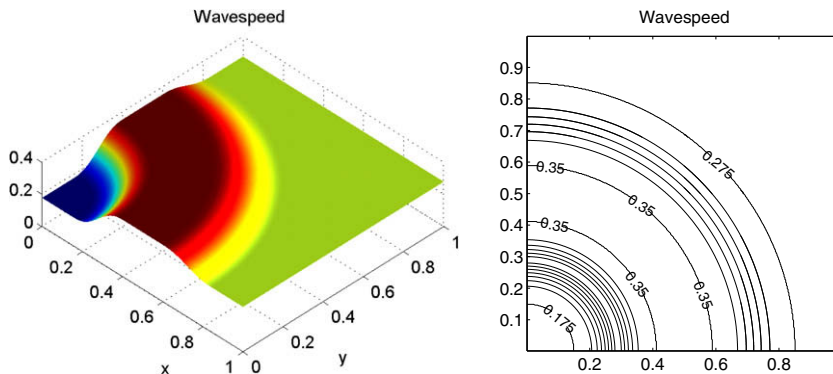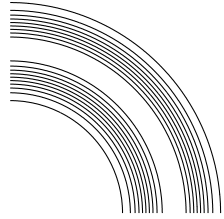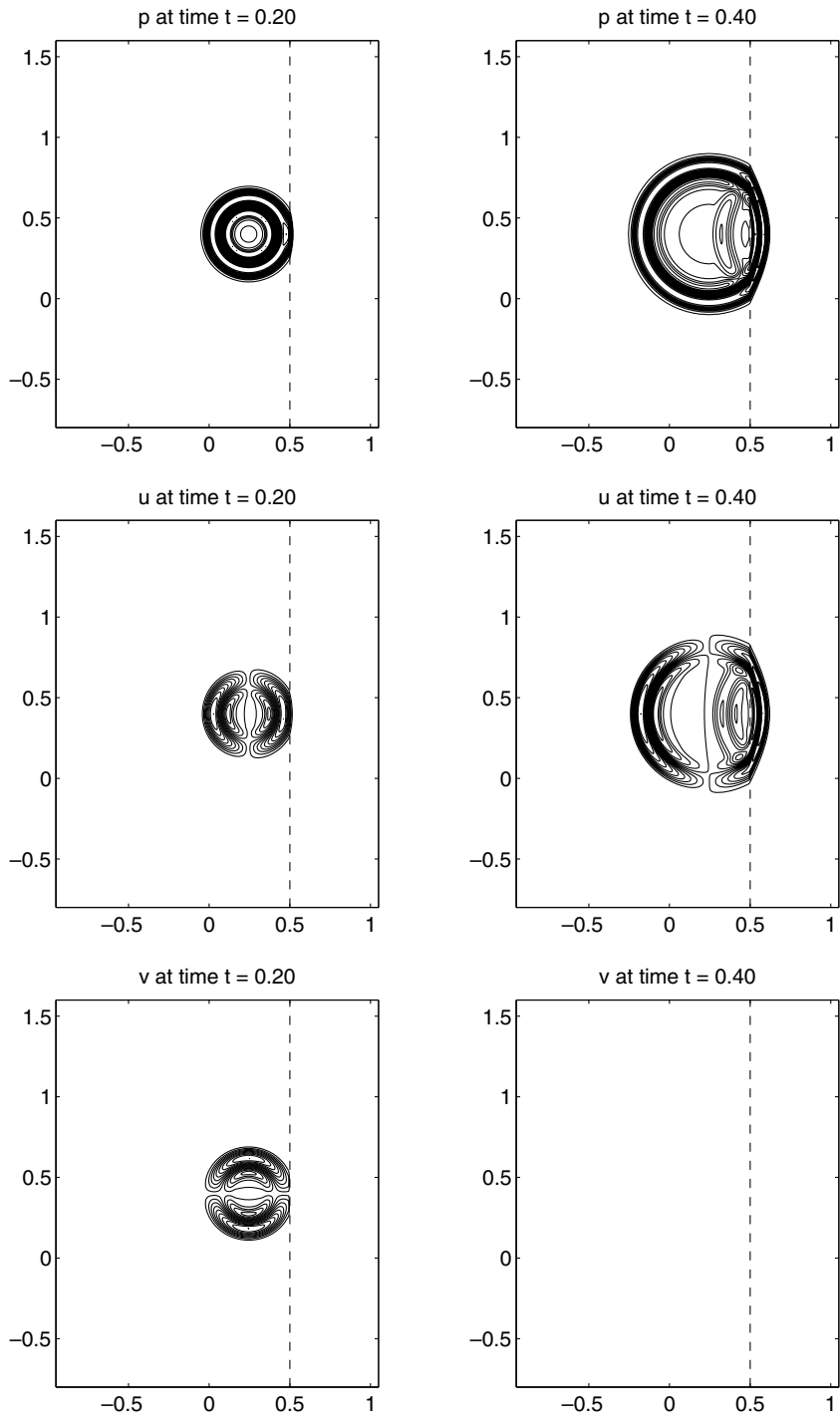

**Fig. 12.** Radially symmetric wave speed a_0.

In the following Tables 5 and 6 the experimental order of convergence is computed by comparing the L^1 errors of two succeeding solutions for the FVEG and the Lax-Wendroff scheme, respectively. Numerical experiments again clearly demonstrate the desired second order of convergence of both schemes. Note however, that the FVEG scheme is much more accurate than the Lax-Wendroff scheme. In fact, the error of the FVEG scheme is about 10 times smaller than that of the Lax-Wendroff scheme.

5.2.1. Wave propagation in a medium with radially symmetric wave speed

In this example that is motivated by LeVeque [1] we model the wave propagation in a radially symmetric medium. The wave speed a_0 is a C^2 function obtained by polynomial blending of the following constant states
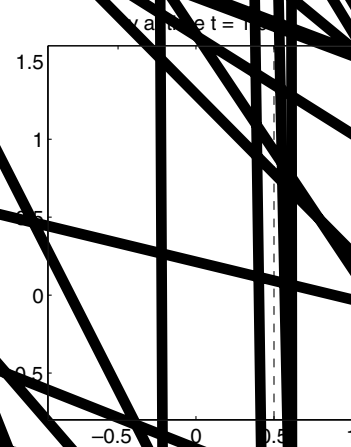
$$a_0(r) = \begin{cases} 0.175 & \text{if} \quad r \leqslant 0.15 \\ 0.350 & \text{if} \quad 0.41 < r \leqslant 0.59 , \\ 0.275 & \text{if} \quad 0.85 < r \end{cases}$$

with the radius $r = \sqrt{x^2 + y^2}$.
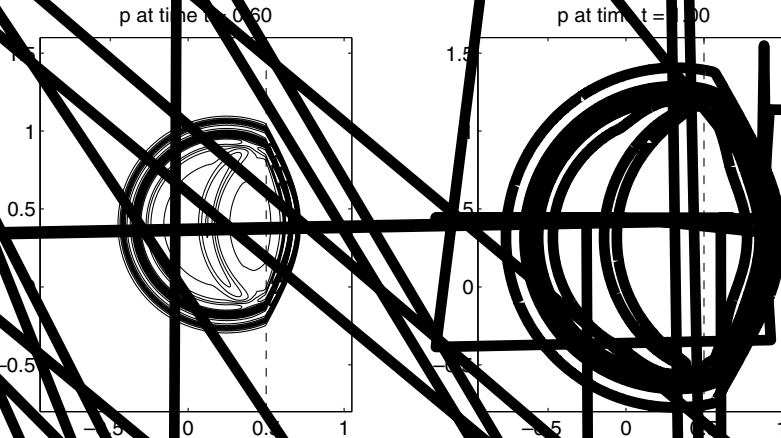
Table 5
L^1 errors and experimental order of convergence of the FVEG scheme; Example 5.2.1.

N	N_{ref}	L^1 error of p	EOC	L^1 error of u	EOC	L^1 error of $\rho_0 u$	EOC
25	50	3.32e−02		1.23e−02		2.06e−02	
50	100	8.66e−03	1.937	3.20e−03	1.935	5.83e−03	1.822
100	200	1.65e−03	2.390	5.87e−04	2.449	1.08e−03	2.432
200	400	3.05e−04	2.439	1.32e−04	2.153	2.28e−04	2.247
400	800	6.40e−05	2.249	3.28e−05	2.009	5.44e−05	2.063
800	1600	1.48e−05	2.111	8.33e−06	1.976	1.38e−05	1.983
1600	3200	3.59e−06	2.046	2.11e−06	1.979	3.50e−06	1.975

N	N_{ref}		L^1 error of v	EOC	L^1 error of $\rho_0 v$	EOC
25	50		1.53e−02		2.17e−02	
50	100		3.82e−03	2.001	6.01e−03	1.852
100	200		7.37e−04	2.373	1.23e−03	2.284
200	400		1.55e−04	2.246	2.57e−04	2.263
400	800		3.81e−05	2.028	6.23e−05	2.043
800	1600		9.65e−06	1.980	1.58e−05	1.981
1600	3200		2.44e−06	1.982	4.01e−06	1.977

Table 6
L^1 errors and experimental order of convergence of the Lax-Wendroff scheme; Example 5.2.1.

N	N_{ref}	L^1 error of p	EOC	L^1 error of u	EOC	L^1 error of $\rho_0 u$	EOC
25	50	1.00e−01		3.75e−02		6.00e−02	
50	100	2.27e−02	2.142	2.17e−02	0.792	3.46e−02	0.793
100	200	8.40e−03	1.434	4.75e−03	2.189	7.92e−03	2.128
200	400	2.13e−03	1.977	1.16e−03	2.029	1.99e−03	1.995
400	800	5.32e−04	2.003	2.90e−04	2.003	5.00e−04	1.991
800	1600	1.33e−04	1.997	7.24e−05	2.002	1.25e−04	1.999
1600	3200	3.33e−05	1.998	1.81e−05	2.001	3.13e−05	1.999

N	N_{ref}		L^1 error of v	EOC	L^1 error of $\rho_0 v$	EOC
25	50		4.49e−02		6.37e−02	
50	100		2.26e−02	0.990	3.44e−02	0.888
100	200		4.80e−03	2.235	7.76e−03	2.148
200	400		1.14e−03	2.075	1.88e−03	2.044
400	800		2.81e−04	2.020	4.67e−04	2.009
800	1600		6.98e−05	2.007	1.16e−04	2.004
1600	3200		1.74e−05	2.002	2.91e−05	2.001

Table 7
L^1 errors and experimental order of convergence for the test with radially symmetric wave speed by the FVEG scheme.

N	N_{ref}	L^1 error of p	EOC	L^1 error of u	EOC	L^1 error of $\rho_0 u$	EOC
25	50	2.58e−02		3.47e−03		6.85e−02	
50	100	5.29e−03	2.287	6.72e−04	2.369	1.44e−02	2.255
100	200	8.41e−04	2.651	1.08e−04	2.635	2.37e−03	2.599
200	400	1.37e−04	2.614	1.88e−05	2.526	4.29e−04	2.465
400	800	2.69e−05	2.352	4.04e−06	2.215	9.37e−05	2.194
800	1600	6.39e−06	2.072	9.92e−07	2.026	2.32e−05	2.010
1600	3200	1.61e−06	1.991	2.50e−07	1.987	5.91e−06	1.975

Table 8
L^1 errors and experimental order of convergence for the test with radially symmetric wave speed by the Lax-Wendroff scheme.

N	N_{ref}	L^1 error of p	EOC	L^1 error of u	EOC	L^1 error of $\rho_0 u$	EOC
25	50	7.12e−02		8.91e−03		1.57e−01	
50	100	2.44e−02	1.545	3.00e−03	1.569	6.03e−02	1.384
100	200	6.81e−03	1.842	8.28e−04	1.858	1.75e−02	1.786
200	400	1.79e−03	1.929	2.16e−04	1.939	4.62e−03	1.917
400	800	4.45e−04	2.005	5.36e−05	2.009	1.16e−03	1.992
800	1600	1.09e−04	2.028	1.32e−05	2.026	2.85e−04	2.026
1600	3200	2.72e−05	2.005	3.27e−06	2.006	7.11e−05	2.002

The isentropic exponent γ is set to 1.4. The background pressure is $p_0 = 1.0$ and the initial pressure is a C^2 function given in the following way:

$$\bar{p}(x) := -2x^6 + 6x^4 - 6x^2 + 2$$

$$p(x,y) = \begin{cases} \bar{p}((r - 0.5)/0.18) & \text{if} \quad |r - 0.5| < 0.18 \\ 0 & \text{otherwise}. \end{cases}$$

The computational domain is $[-1; 1] \times [-1; 1]$. Absorbing boundary conditions are implemented by extrapolating all components of the solution, see also [21] for other techniques in order to implement absorbing boundary conditions. Due to symmetry arguments the test was performed on the computational domain $[0; 1] \times [0; 1]$ with symmetric boundary conditions at the lower and left boundaries. The final time is $t = 1.0$. The results of the experimental order of convergence are given in the Table 7. Due to the radial symmetry the errors for u and v are identical within the given precision. Table 8 shows the errors and convergence rates obtained by the Lax-Wendroff scheme. Analogously as in the previous example we can clearly see much better accuracy of the FVEG scheme in comparison with the standard second order finite difference scheme.
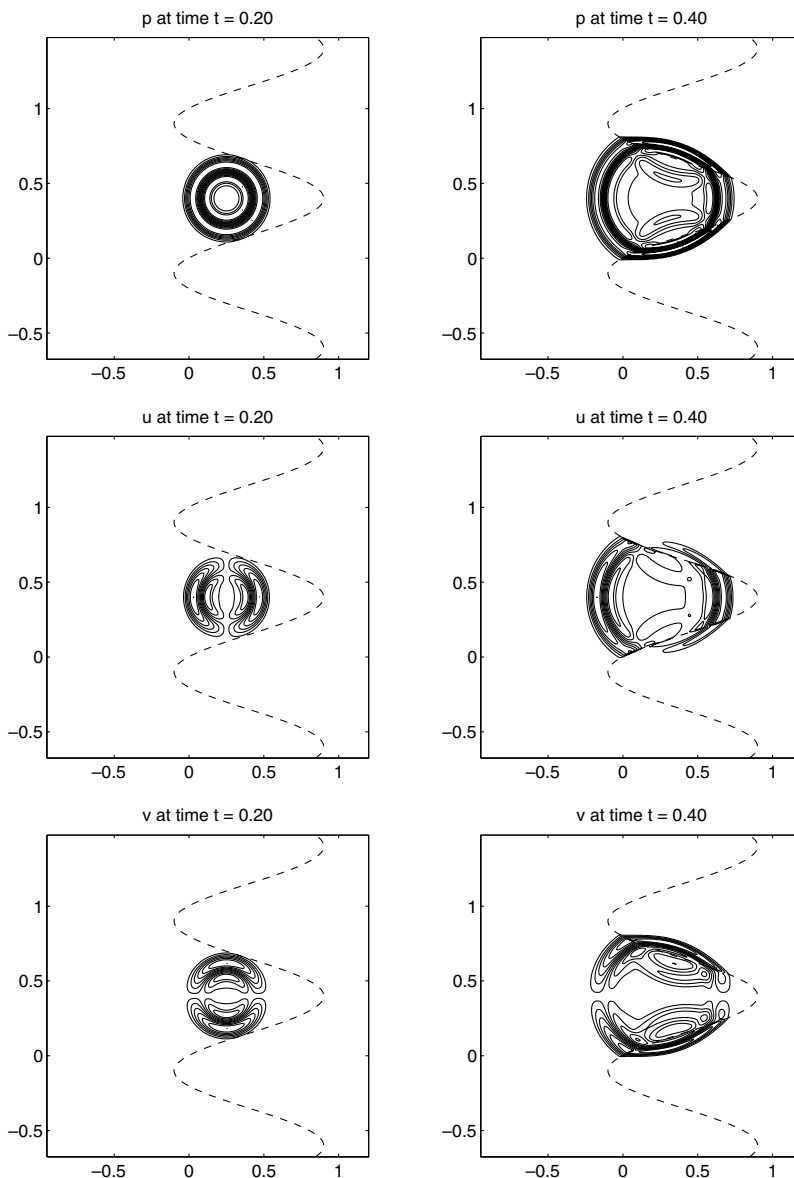

Fig. 16. Solution isolines for $t = 0.2$ and $t = 0.4$, curved interface.

5.2.3. Wave propagation in a heterogeneous medium with discontinuous wave speed

In this experiment we model the propagation of acoustic waves through a layered medium with a single interface. The piecewise constant wave speed is given as follows:

$$a_0(x,y) = \begin{cases} 1.0 & \text{if} \quad x < 0.5 \\ 0.5 & \text{otherwise}. \end{cases}$$

The initial data are

$$p(x,y) = \begin{cases} 1.0 + 0.5(\cos(\pi r/0.1) - 1.0) & \text{if} \quad r < 0.1 \\ 0 & \text{otherwise}, \end{cases}$$

$$u(x,y) = 0 = v(x,y),$$

where the radius r is given by $r := \sqrt{(x - 0.25)^2 + (y - 0.4)^2}$. We set $\gamma = 1.0$, $p_0 = 1.0$ and the final time $t = 1.0$. The computational domain is $[-0.95; 1.05] \times [-0.8; 1.6]$. The absorbing boundary conditions are implemented by extrapolating all components of solution. In this experiment we use the monotonized minmod limiter in bilinear recovery. In
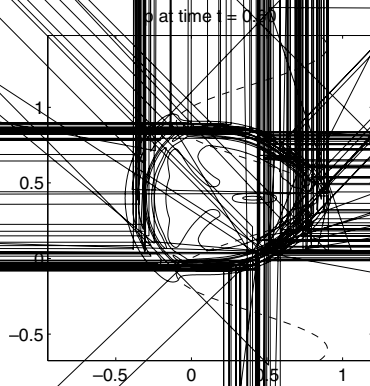
isolines of pressure and velocities in *x*- and *y*-directions are depicted at several time steps. We can notice good resolution of circular waves as well as a typical change of the wave form as the pulse propagates through the medium interface.

5.2.4. Wave propagation in a heterogeneous medium with complex interface
The aim of this experiment is to illustrate capability of the FVEG method to model a wave propagation in heterogenous medium having complex interface not aligned to the grid. Now, the piecewise constant wave speed is defined as

$$a_0(x,y) = \begin{cases} 1.0 & \text{if } x \leqslant 0.5\cos(2\pi(y-0.4)) + 0.4 \\ 0.5 & \text{otherwise}. \end{cases}$$

The computational domain is chosen to be $[-0.95; 1.2] \times [-0.675; 1.475]$ and initial data are defined in the same way as in the previous example.

In Figs. 16 and 17 isolines of pressure and velocities in *x*- and *y*-directions are depicted at different time instances. Similarly as before we can clearly observe a change in the shape of circular waves as they propagate into the different medium. Moreover, due to the curved interface a complex pattern of reflection waves can be noticed. They are superposed over the propagating waves as follows from the linearity of the wave equation system.

6. Conclusions

In this paper we have generalized the genuinely multi-dimensional finite volume evolution Galerkin (FVEG) scheme to hyperbolic conservation laws with spatially varying flux functions. The methodology has been presented for acoustic waves in heterogeneous medium. The FVEG scheme is based on multi-dimensional approximate evolution operator that is used for prediction of fluxes on cell interfaces. Using general theory of bicharacteristics we have derived in the Sections 2 and 3 new approximate evolution operators for spatially varying fluxes without any local linearization. This is a novel feature of the present paper. A staggered grid approach is used to approximate heterogeneous medium. As a consequence this approach reduces oscillations at the interface where the wave speed is discontinuous. Numerical results for wave propagation with continuous as well as discontinuous wave speeds demonstrate correct numerical resolution, second order convergence rate and much better global accuracy in comparison to some standard finite difference schemes. In future we would like to generalize ideas presented in this paper to more complex hyperbolic conservation laws with spatially varying fluxes.

Appendix A. Exact wavefront for linear wave speed

Let the wave velocity a_0 be a linear function of the form

$$a_0(x,y) = \bar{a}_0 + a_{0x}(x-x_P) + a_{0y}(y-y_P), \tag{A.1}$$

where (x_P, y_P) is a fixed point. In the FVEG scheme $(x_P, y_P) = (x(t_{n+1}), y(t_{n+1}))$ corresponds to the apex of characteristic conoid. In this case the wavefront, the bicharacteristics and the corresponding time steps that fulfill the CFL condition can be calculated analytically.

Lemma A.1. *Let a_0 be defined by (A.1). Then the solution of the system*

$$\begin{aligned}
\frac{dx}{dt} &= -a_0(x,y)\cos\theta, \quad x(t_{n+1}) = x_P, \\
\frac{dy}{dt} &= -a_0(x,y)\sin\theta, \quad y(t_{n+1}) = y_P, \\
\frac{d\theta}{dt} &= -a_{0x}\sin\theta + a_{0y}\cos\theta, \quad \theta(t_{n+1}) = \omega
\end{aligned} \tag{A.2}$$

is described by the following formulae as long as the wave speed $a_0(x,y)$ along a bicharacteristic stays positive. Let $t_n \leqslant \tau < t_{n+1}$.

- If $a_{0x} = a_{0y} = 0$ then the solution is

$$\begin{bmatrix} x(\tau, \omega) \\ y(\tau, \omega) \end{bmatrix} = \begin{bmatrix} x_P \\ y_P \end{bmatrix} + \bar{a}_0(t_{n+1} - \tau) \begin{bmatrix} \cos \omega \\ \sin \omega \end{bmatrix}, \tag{A.3}$$

and

$$\theta(\tau, \omega) = \omega. \tag{A.4}$$

- If $a_{0x} \neq 0$ or $a_{0y} \neq 0$ then using the polar transformation

$$(r \cos(\varphi), r \sin(\varphi)) := (a_{0x}, a_{0y}),$$

the solution is

$$\begin{bmatrix} x(\tau, \omega) \\ y(\tau, \omega) \end{bmatrix} = \begin{bmatrix} x_P \\ y_P \end{bmatrix} + \frac{\bar{a}_0}{r}(\cosh(r(t_{n+1} - \tau)) - 1) \begin{bmatrix} \cos \varphi \\ \sin \varphi \end{bmatrix} + \frac{\bar{a}_0}{r} \sinh(r(t_{n+1} - \tau)) \begin{bmatrix} \cos \theta(\tau, \omega) \\ \sin \theta(\tau, \omega) \end{bmatrix}, \tag{A.5}$$

and

$$\theta(\tau, \omega) = \begin{cases} \varphi + 2 \arctan \left(e^{r(t_{n+1} - \tau)} \tan \left(\frac{\omega - \varphi}{2} \right) \right) & \text{if} \quad \omega - \varphi \neq (2k+1)\pi, \quad k \in \mathbb{Z} \\ \omega & \text{if} \quad \omega - \varphi = (2k+1)\pi, \quad k \in \mathbb{Z}. \end{cases} \tag{A.6}$$

Proof. Follows from direct, but tedious, derivation of solution of the ODE system (A.2). Note that $\theta(\tau) = \omega$ when $\gamma = 0$ and when $\omega - \varphi = (2k+1)\pi, k \in \mathbb{Z}$. $\quad \square$

Remark A.1. For a fixed φ, τ and $\gamma \neq 0$ the function $\theta(\tau, \cdot)$ is continuous and $\theta(\tau, 0) = \theta(\tau, \pi)$. The backward characteristic conoid through the point (x_P, y_P) is given parametrically by (A.5) as τ and ω vary as seen in Fig. 18.

We would like to thank the unknown referee for pointing out that the fact that rays are circles when gradients are constant is a well-known result, cf., e.g., [6].

Lemma A.2. Let r and φ be defined as in Lemma A.1 and ν be the CFL number. Then the time step satisfying the CFL stability condition is given as follows:

- If $a_{0x} = a_{0y} = 0$ then

$$\Delta t \leqslant \min \left(\frac{\nu \Delta x}{\bar{a}_0}, \frac{\nu \Delta y}{\bar{a}_0} \right). \tag{A.7}$$

- If $a_{0x} \neq 0$ or $a_{0y} \neq 0$ then by setting

$$\alpha_{\Delta x} := |\cos(\varphi)|, \quad \alpha_{\Delta y} := |\sin(\varphi)|$$
$$\beta_{\Delta x} := \frac{\nu r \Delta x}{a_0(x_P, y_P)},$$
$$p_{\Delta x} := \frac{\alpha_{\Delta x} + \beta_{\Delta x}}{\alpha_{\Delta x} + 1} + \sqrt{\left(\frac{\alpha_{\Delta x} + \beta_{\Delta x}}{\alpha_{\Delta x} + 1} \right)^2 - \frac{\alpha_{\Delta x} - 1}{\alpha_{\Delta x} + 1}},$$

and $p_{\Delta y}$ and $\beta_{\Delta y}$ analogously to $p_{\Delta x}$ and $\beta_{\Delta x}$ the time step is bounded by
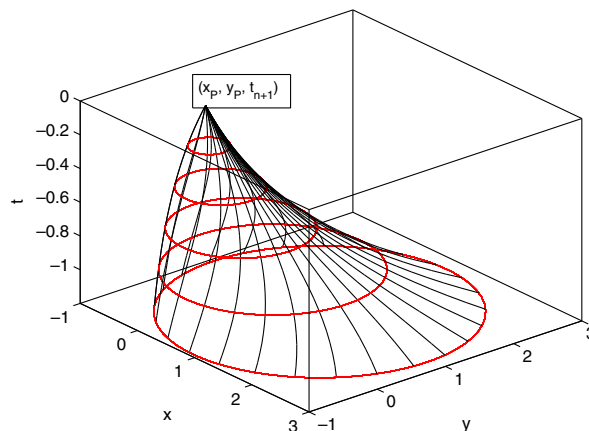

Fig. 18. Exact characteristic conoid for $r = \sqrt{2}, \ \phi = \pi/4$.
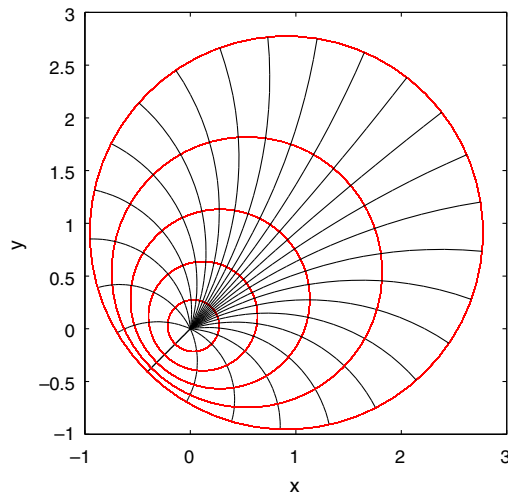
Fig. 19. Exact rays and wavefronts for $r = \sqrt{2}$, $\phi = \pi/4$.

$$\Delta t \leqslant \min(\ln(p_{\Delta x}), \ln(p_{\Delta y}))/r. \tag{A.8}$$

Proof. Follows from the results of Lemma A.1 □

Remark A.2. The analytic formulae for the CFL condition (A.7), (A.8) are sensitive to the finite precision of floating point arithmetic. In particular it means that if the slope of a_0 is close to zero the time steps of zero can be obtained from (A.8) by finite precision. For example, assume for a one-dimensional problem without loss of generality $\alpha_{\Delta x} = 1$. Then $\beta_{\Delta x} \ll 1$ gives $p_{\Delta x} \approx 1$ and thus Δt becomes very small. In order to cure this we need to give a threshold value to turn to the formula (A.7) if the slope of a_0 is less then the threshold.

Numerical tests indicate that the formulae from Lemma A.1 applied to linearly recovered wave speeds give only in high resolutions a slight advantage of accuracy. In fact, we can show by the Taylor expansion of exact wavefront (A.5),(A.6) with respect to τ that its radius differs only to third order and its center to second order accuracy from the approximations used in Section 3. But the formulae (A.5),(A.6) are more complicated and more expensive computationally. Therefore, in general it is advisable to work with the approximate wavefront given in (3.10).

Finally let us illustrate a characteristic conoid, rays and wavefronts for a_0 given by (A.1), cf. Figs. 18 and 19, where $t_{n+1} = 0, t_n = -1.2, \bar{a}_0 = 1$ and $r = \sqrt{2}, \phi = \pi/4$.

Appendix B. Supplementary data

Supplementary data associated with this article can be found, in the online version, at doi:10.1016/j.jcp.2008.10.004.

References

[1] D.S. Bale, R.J. LeVeque, S. Mitran, J.A. Rossmanith, A wave propagation method for conservative laws and balance laws with spatially varying flux functions, SIAM J. Sci. Comput. 24 (2002) 955–978.
[2] A. Bayliss, K.E. Jordan, B.J. LeMesurier, E. Turkel, A fourth-order accurate finite-difference scheme for the computation of elastic waves, Bull. Seism. Soc. Am. 76 (1986) 1115–1132.
[3] D. Boore, Finite-difference methods for seismic wave propagation in heterogeneous materials, in: B.A. Bolt (Ed.), Methods in Computational Physics, vol. 11, Academic Press, New York, 1972.
[4] D.S. Butler, The numerical solution of hyperbolic systems of partial differential equations in three independent variables, Proc. Roy. Soc. 225A (1960) 233–252.
[5] R. Courant, D. Hilbert, Methods of Mathematical Physics, Interscience Publishers, 1962.
[6] C. Chapman, Fundamentals of Seismic Wave Propagation, Cambridge University Press, 2004.
[7] S.H. Emerman, W. Schmidt, R.A. Stephen, An implicit finite-difference formulation of the elastic wave equation, Geophysics 47 (1982) 1521–1526.
[8] T.R. Fogarty, Finite Volume Methods for Acoustics and Elasto-plasticity with Damage in Heterogeneous Material, PhD Thesis, University of Washington, 2001.
[9] T.R. Fogarty, R.J. LeVeque, High-resolution finite volume methods for acoustics in periodic or random media, J. Acoust. Soc. Am. 106 (1999) 17–28.
[10] R. Glowinski, A. Bamberger, Q.H. Tran, A domain decomposition method for the acoustic wave equation with discontinuous coefficients and grid change, SIAM J. Numer. Anal. 34 (2) (1997) 603–639.
[11] T. Kröger, M. Lukáčová-Medvid'ová, An evolution Galerkin scheme for the shallow water magnetohydro-dynamic (SMHD) equations in two space dimensions, J. Comp. Phys. 206 (2005) 122–149.
[12] A.R. Levander, Fourth-order finite-difference P–SV seismograms, Geophysics 53 (1988) 1425–1436.

[13] R.J. LeVeque, Finite Volume Methods for Hyperbolic Problems, Cambridge University Press, Cambridge, 2002.
[14] R.J. LeVeque, Finite volume methods for nonlinear elasticity in heterogeneous media, in: Proceedings of the ICFD Conference on Numerical Methods for Fluid Dynamics, Oxford University, March 2001.
[15] P. Lin, K.W. Morton, E. Süli, Euler characteristic Galerkin scheme with recovery, M^{2}AN 27 (1993) 863–894.
[16] P. Lin, K.W. Morton, E. Süli, Characteristic Galerkin schemes for scalar conservation laws in two and three space dimensions, SIAM J. Numer. Anal. 34 (1997) 779–796.
[17] M. Lukáčová-Medvid'ová, K.W. Morton, G. Warnecke, Evolution Galerkin methods for hyperbolic systems in two space dimensions, Math. Comp. 69 (2000) 1355–1384.
[18] M. Lukáčová-Medvid'ová, J. Saibertová, G. Warnecke, Finite volume evolution Galerkin methods for nonlinear hyperbolic systems, J. Comp. Phys. 183 (2002) 533–562.
[19] M. Lukáčová-Medvid'ová, K.W. Morton, G. Warnecke, Finite volume evolution Galerkin (FVEG) methods for hyperbolic problems, SIAM J. Sci. Comput. 26 (2004) 1–30.
[20] M. Lukáčová-Medvid'ová, S. Noelle, M. Kraft, Well-balanced finite volume evolution Galerkin methods for the shallow water equations, J. Comp. Phys. 221 (2007) 122–147.
[21] M. Lukáčová-Medvid'ová, G. Warnecke, Y. Zahaykah, On the boundary conditions for EG-methods applied to the two-dimensional wave equation systems, J. Appl. Mech. Math. (ZAMM) 84 (4) (2004) 237–251.
[22] M. Lukáčová-Medvid'ová, G. Warnecke, Y. Zahaykah, On the stability of evolution Galerkin schemes applied to a two-dimensional wave equation system, SIAM J. Numer. Anal. 44 (2006) 1556–1583.
[23] K. Mattsson, J. Nordström, High order finite difference methods for wave propagation in discontinuous media, J. Comp. Phys. 220 (2006) 249–269.
[24] P. Moczo, J.O.A. Robertsson, L. Eisner, The finite-difference time-domain method for modelling of seismic wave propagation, in: R.-S. Wu, V. Maupin (Eds.), Advances in Wave Propagation in Heterogeneous Earth, Advances in Geophysics, vol. 48, Elsevier, Academic Press, 2007, pp. 421–516.
[25] K.W. Morton, P.L. Roe, Vorticity-preserving Lax-Wendroff-type schemes for the system wave equation, SIAM J. Sci. Comput. 23 (1) (2001) 170–192.
[26] S. Ostkamp, Multidimensional characteristic Galerkin schemes and evolution operators for hyperbolic systems, Math. Meth. Appl. Sci. 20 (1997) 1111–1125.
[27] P. Prasad, On the lemma on bicharacteristics, Appendix in "A nonlinear ray theory, Berichte der Arbeitsgruppe Technomathematik, Universität Kaiserslautern, Nr. 101, 1993.
[28] P. Prasad, Nonlinear Hyperbolic Waves in Multidimensions, Monographs and Surveys in Pure and Applied Mathematics, Chapman & Hall/CRC, 2001.
[29] P. Prasad, Ray theories for hyperbolic waves, kinematical conservation laws (KCL) and applications, Ind. J. Pure Appl. Math. 38 (2007) 467–490.
[30] P. Prasad, A general version of the extended useful lemma, 2007, private communication.
[31] P. Prasad, R. Ravindran, Canonical form of a quasilinear hyperbolic system of first order equations, J. Math. Phys. Sci. 18 (1984) 361–364.
[32] A.S. Reddy, V.G. Tikekar, P. Prasad, Numerical solution of hyperbolic equations by method of bicharacteristics, J. Math. Phys. Sci. 16 (1982) 575–603.
[33] E.H. Saenger, T. Bohlen, Finite-difference modeling of viscoelastic and anisotropic wave propagation using the rotated staggered grid, Geophysics 69 (2004) 583–591.
[34] J. Virieux, SH-wave propagation in heterogeneous media: velocity–stress finite-difference method, Geophysics 49 (1984) 1933–1957.